16

Suppe, J., C. D. Connors, and Y. Zhang, 2004, Shear fault-bend folding, *in* K. R. McClay, ed., Thrust tectonics and hydrocarbon systems: AAPG Memoir 82, p. 303–323.

Shear Fault-bend Folding

John Suppe

Department of Geosciences, Princeton University, Princeton, New Jersey, U.S.A.

Christopher D. Connors

Department of Geology, Washington and Lee University, Lexington, Virginia, U.S.A.

Yikun Zhang[1]

Department of Geosciences, Princeton University, Princeton, New Jersey, U.S.A.

ABSTRACT

Shear fault-bend folding produces ramp anticlines with very distinctive shapes. They are characterized by long, gentle backlimbs that dip less than the fault ramp, in contrast with classical fault-bend folding. Backlimb dips and limb lengths increase progressively with fault slip, by a combination of limb rotation and kink-band migration. We summarize and apply two simple end-member theories of shear fault-bend folding involving a weak décollement layer of finite thickness at the base of a ramp: (1) simple-shear fault-bend folding, in which the layer undergoes an externally imposed bedding-parallel simple shear with no basal fault, and (2) pure-shear fault-bend folding, in which this basal layer slides above a basal fault and shortens and thickens above the ramp, with no externally applied bed-parallel simple shear. In the limit of large displacement, the fold geometry in pregrowth strata approaches the geometry of classical fault-bend folding, with a backlimb dip that approaches the ramp dip. However, even in these cases, growth strata may record the history of limb rotation that is characteristic of a shear fault-bend fold heritage. We demonstrate that these theories are in agreement with well-imaged seismic examples from the Nankai Trough and Cascadia accretionary wedges, which show substantial shears (40–65°) over stratigraphic intervals of a few hundred meters.

INTRODUCTION

There has been a long-standing intuition that thrust sheets might undergo substantial internal deformation even while they are displaced over their footwalls. This intuition is exemplified by Figure 1, a diagram from David Elliott (1976) showing a ramp anticline— what might now be called a fault-bend fold— with significant layer-parallel simple shear but negligible layer-parallel shortening and thickening (pure shear) within the hanging wall. Indeed, internal deformation in this drawing dominates over basal fault slip in the total displacement of the hanging wall, leading to an output fault slip that exceeds the input fault slip, in spite of the fact that the folding itself consumes slip.

Without discussing the mechanical motivation and merits of this intuition of important internal deformation, suffice it to say that if such internal deformation

[1]*Present address*: Department of Earth Sciences, Nanjing University, Nanjing, China.

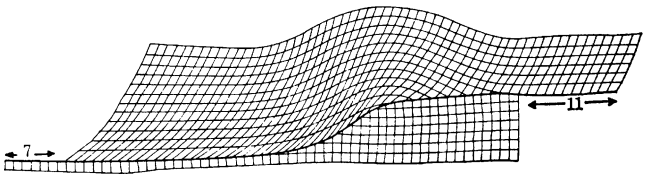

FIGURE 1. There has been a long-standing intuition that thrust sheets might undergo substantial internal deformation even as they are displaced over their footwalls. This schematic ramp anticline from Elliott (1976) exemplifies this intuition by showing the possibility of substantial internal deformation of the hanging wall, in addition to that directly associated with fault displacement. The contributions of layer-parallel simple shear to the displacement of the top of the model (9 units) dominate over the input fault slip (7 units), which leads to an output fault slip (11 units) that is greater than the input, in spite of the fact that folding consumes fault slip.

exists, then the resulting shapes of ramp anticlines should be sensitive to the proportions of fault slip, simple shear, and pure shear. Because of this potential importance, the original balanced theories of fault-bend and fault-propagation folding explicitly included the possibility of layer-parallel simple shear (Suppe, 1983; Suppe and Medwedeff, 1990). Shear in fault-related folds has been considered theoretically by many authors, including Jamison (1987), Mitra and Namson (1989), Mitra (1990, 1992), Mosar and Suppe (1991), Poblet and McClay (1996), Storti and Poblet (1997), and Tamagawa et al. (1998).

In contrast with this substantial theoretical effort, it is remarkable that most successful, rigorous applications of fault-related folding theory to well-documented structures have involved no shear. Most cases in our experience match the no-shear theory rather closely when the fault shape and fold shape are both well constrained by data (one possible but not wholly convincing exception is given in Suppe, 1984). For example, Mitra (1992, 1988) points out that a well-constrained cross section of the Pine Mountain thrust sheet in the southern Appalachians deviates from classical no-shear fault-bend folding by about 1° (with a ramp angle of 17°, the no-shear theory predicts a front-limb dip of 18.8°, whereas the observed frontlimb dip is 18°). This discrepancy from a perfect no-shear solution could result from a forward shear in the frontlimb of about 5° (Figure 2), which would be difficult to prove unequivocally. Mitra did not assign this discrepancy to shear; he suggested that the small deviation might be an effect of dilation as a result of fracturing in the hanging wall.

Mitra's Pine Mountain example is typical of many well-constrained structures in fold-and-thrust belts in which externally imposed layer-parallel shear has been found to be second-order or absent, presumably reflecting the fact that thrust faults are commonly much weaker than their hanging walls (cf. Davis et al., 1983). Rather than further document such examples of negligible shear, it is the purpose of this chapter to show that there are some widespread thrust-belt environments in which hanging-wall shear is a very important process. In particular, we summarize simple end-member theories of pure-shear and simple-shear fault-bend folding following Suppe (2004). We then show that several well-imaged seismic examples from the deep-water Nankai Trough and Cascadia accretionary wedges agree closely with shear fault-bend fold theory, with shears of 40–65° over stratigraphic intervals of a few hundred meters.

CLASSICAL FAULT-BEND FOLDING WITH SIMPLE SHEAR

Fault-related fold theories involving layer-parallel simple shear are most easily developed using the concept of effective-cutoff and fault-bend angles. Effective-cutoff and fault-bend angles are the angles that would exist if we could apply the shear before folding. If we use effective angles rather than the actual angles, then classical no-shear fault-bend folding theory applies immediately without modification. It's that simple.

The concept of effective-cutoff angles is shown in Figure 3. The figure shows a classical fault-bend fold with an externally imposed simple shear, α_e. If, in a thought experiment, we apply this shear before folding, thereby causing a displacement d of the top of the hanging wall, then the fault-bend angle ϕ will be modified to an effective fault-bend angle, ϕ_{ef}, and the initial cutoff angle θ

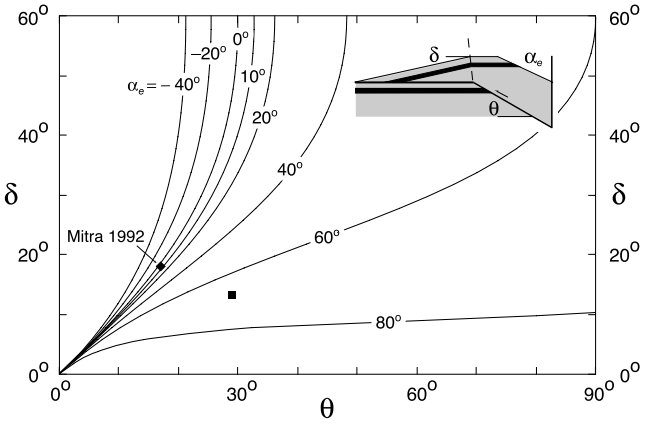

FIGURE 2. Anticlinal fault-bend folding at a ramp-flat transition, including possible externally imposed layer-parallel simple shear α_e. The parameters for the inset schematic fold are shown as the black square. Data for the Pine Mountain thrust sheet from Mitra (1992) deviate slightly from the no-shear theory (with a ramp angle of 17°, the no-shear theory predicts a frontlimb dip of 18.8°, whereas the observed frontlimb dip is 18°). This deviation could result from a forward shear of about 5°, but it would be difficult to prove unequivocally. This example is typical of many structures that show negligible shear.

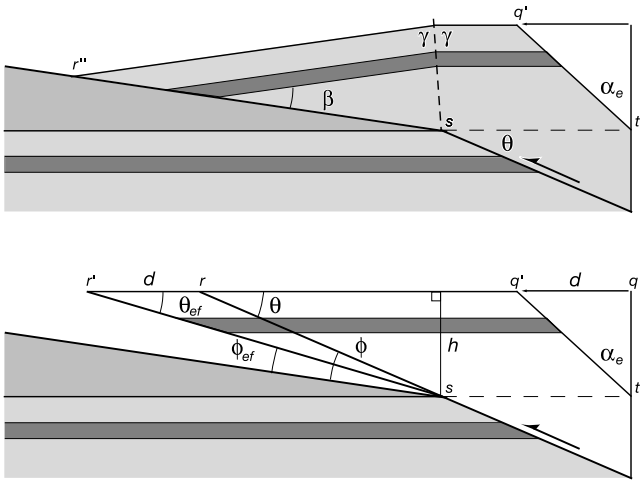

FIGURE 3. Anticlinal fault-bend fold with an externally applied simple shear α_e. The correct balanced fold shape, given the fault shape and shear, can be determined immediately from classical no-shear fault bend folding, if we use *effective-cutoff* θ_{ef} and *fault-bend angles* ϕ_{ef} , rather than the ordinary angles θ and ϕ. The effective angles are those that would exist if we could apply the shear before folding, as shown in the lower figure. Figure 2 was computed using effective angles.

will be modified to an effective-cutoff angle, θ_{ef}. These effective angles may be inserted directly into the no-shear fault-bend fold equations (Suppe, 1983) to compute the fold shape (β, γ). Alternatively, the no-shear fault-bend-folding graph (Figure 7 of Suppe, 1983) can be employed directly to solve subsurface structural problems in cross section, using the effective angles. Variations on this concept of effective angles are used to develop the simple-shear and pure-shear fault-bend-fold theories summarized in this chapter. Figure 2 was computed using effective angles.

SHEAR WITHIN A BASAL DÉCOLLEMENT OF FINITE THICKNESS

The two end-member types of fault-bend folding considered here— pure-shear and simple-shear fault-bend folding— involve distributed deformation of a weak décollement layer of finite thickness at the base of a fault ramp (Figure 4). In simple-shear fault-bend folding, the décollement layer undergoes an externally imposed bedding-parallel simple shear with no basal fault slip. Thus the simple-shear end member has no bedding-parallel fault— just a ramp with slip going to zero at its base. In pure-shear fault-bend folding, this basal layer slides above a basal fault and shortens parallel to bedding and thickens perpendicular to bedding above the ramp,

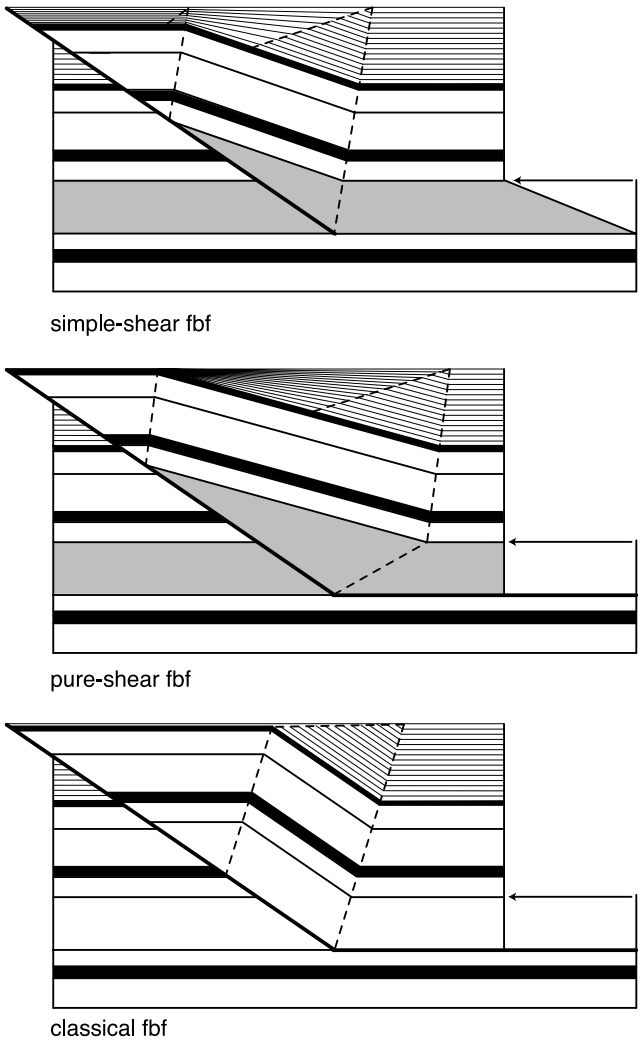

FIGURE 4. Simple-shear and pure-shear fault-bend folds characteristically show backlimb dips that are less than the ramp dip, in contrast with classical no-shear fault-bend folds. The two shear end members involve distributed deformation of a weak décollement layer of finite thickness at the base of a fault ramp, shown in gray. In *simple-shear fault-bend folding,* the décollement layer undergoes an externally imposed bedding-parallel simple shear with no basal fault slip. In *pure-shear fault-bend folding,* this basal layer slides above a basal fault and shortens and thickens above the ramp, with no externally applied simple shear. The growth strata show that shear fault-bend folds undergo a combination of progressive limb rotation and limb lengthening by kink-band migration, whereas classical fault-bend folds grow solely by kink-band migration.

with no externally imposed simple shear. In both cases, the weak layer is overlain by normal strata that conserve layer thickness and bed length and undergo no externally imposed shear.

These two end members correspond to the Type 2 and Type 3 fault-bend folds of Jordan and Noack (1992), who presented some theory of the end members and their

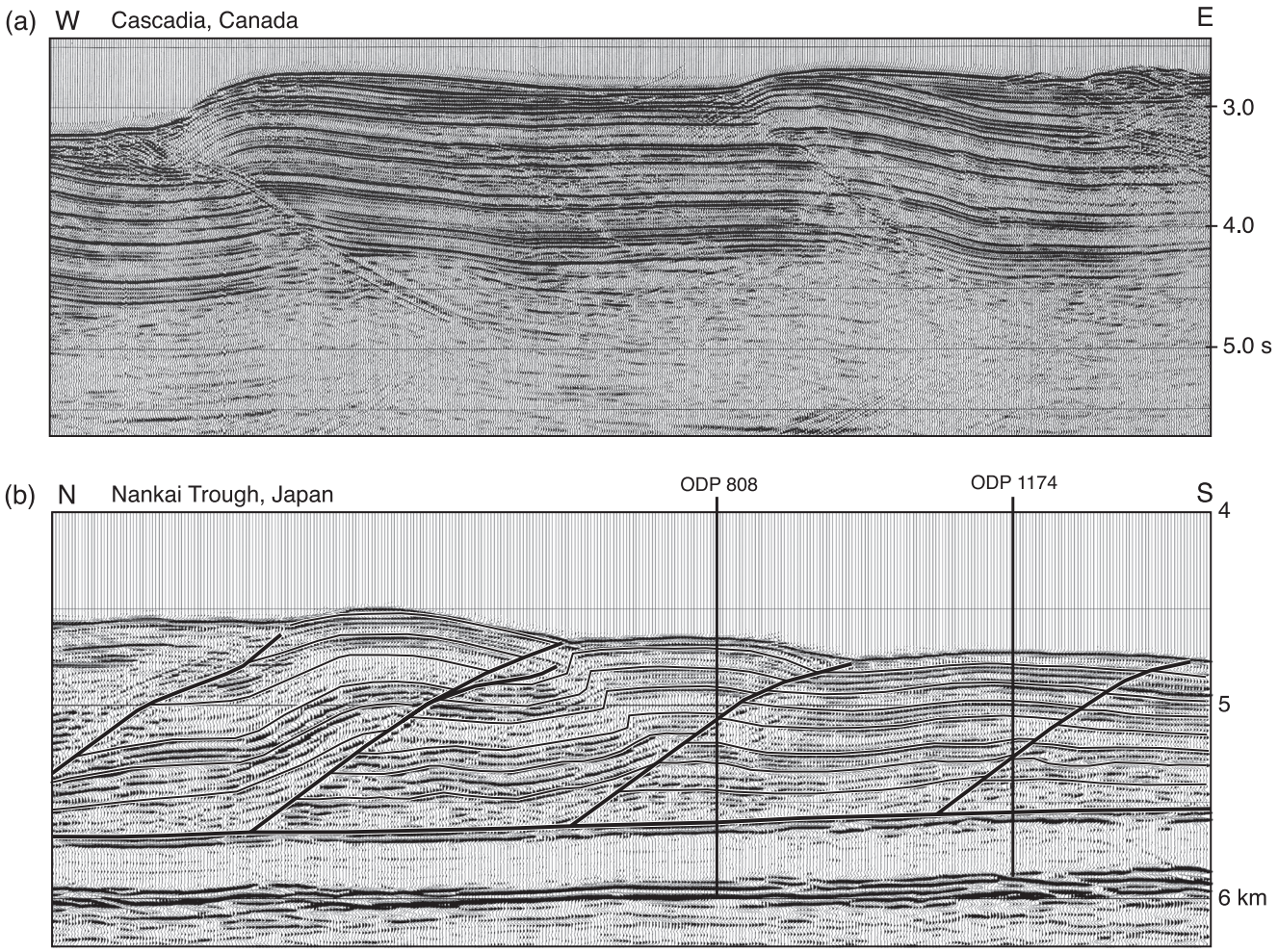

FIGURE 5. These folds display the qualitative characteristics of shear fault-bend folds, including backlimbs that dip much less than the fault dip and a steeply dipping narrow frontlimb. (a) Above is a time section of two ramp anticlines from the Cascadia accretionary wedge, offshore western Canada (line 89-04 of Hyndman et al., 1994). (b) Below is a depth-migrated section (h = v) of line NT62-8 from the Nankai Trough accretionary wedge, offshore Shikoku, Japan (Moore et al. 1990, 1991). This line passes through Ocean Drilling Project sites ODP-808 and ODP-1174 (Moore et al., 1991, 2001; Shipboard Scientific Party, 2001).

more complex intermediates, together with applications involving the basal ductile décollement of the Jura. The idea that simple-shear fault-bend folding involves a basal ductile décollement (Type 2) was, according to Jordan and Noack (1992), first introduced by Malavieille and Ritz (1989) and Taboada et al. (1990), who were primarily concerned with the strain paths within the ductile layer. A simple-shear fault-bend folding theory also was developed by Wayne Narr (personal communication, 1989). Early articulations of pure-shear fault-bend folding include those of Serra (1977) and Suter (1981). A continuous gradation is theoretically possible between a classical fault-bend folding end member and the pure-shear and simple-shear end members, as discussed by Jordan and Noack (1992). They also discussed heterogeneous shear. To our knowledge, the concepts of pure-shear and simple-shear fault-bend folding have not been widely applied. Therefore, this chapter summarizes key elements of a more complete and accessible theory after Suppe (2004) and shows that several well-imaged structures agree well with the theory.

Pure-shear and simple-shear fault-bend folding both produce a fold geometry for ramp anticlines that is normally quite different from classical fault-bend folding (Figure 4). They display backlimb dips that are shallower—often much shallower— than the fault-ramp dips, yet they may have a steep, narrow frontlimb at the top of the ramp. In contrast, a classical no-shear fault-bend fold stepping up from a décollement will have backlimb dips that are equal to the ramp dip. With excellent seismic data, these contrasting structural styles are easily differentiated. For example, seismic images of fault-related folds of the Cascadia subduction zone of western Canada and the Nankai Trough of Japan (Figure 5) show long, gentle backlimbs, steep fault ramps, and narrow, steep frontlimbs that are quite unlike classical fault-bend folds.

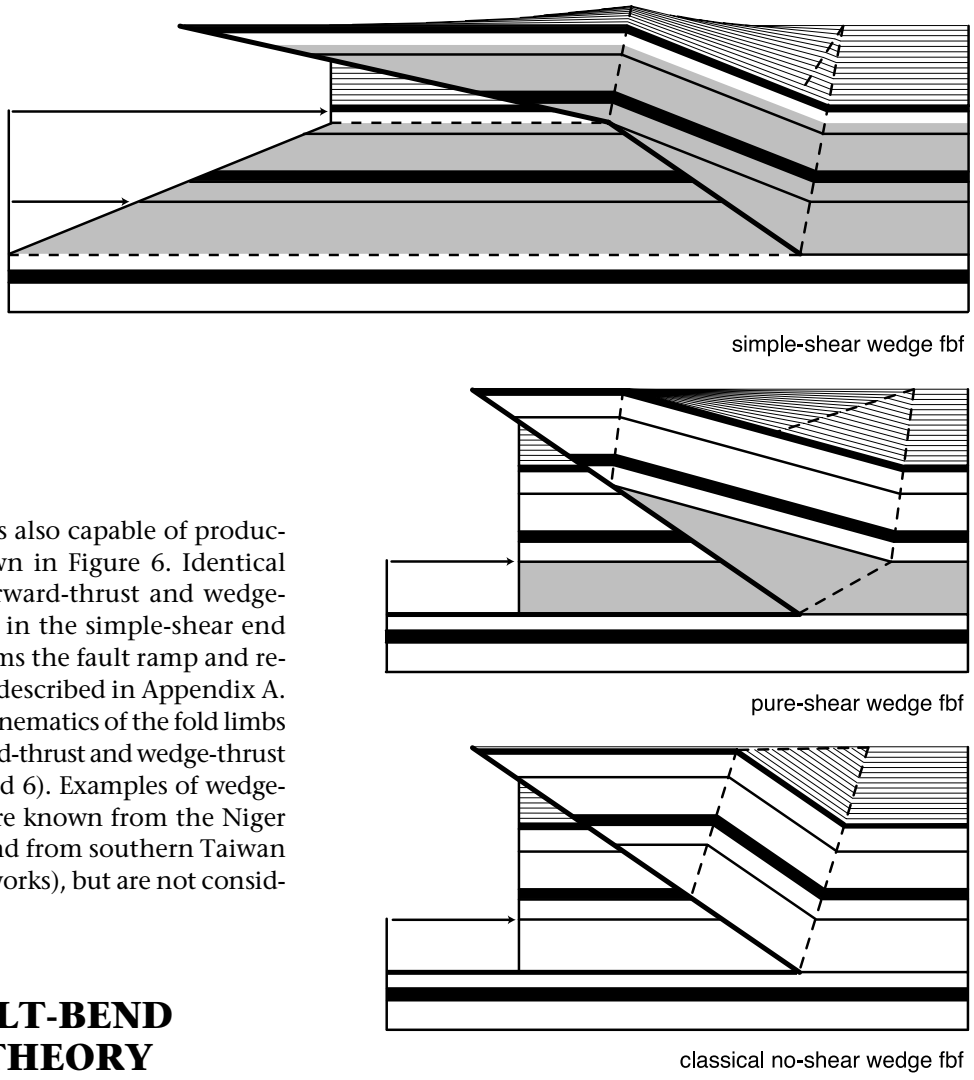

FIGURE 6. Wedge-thrust fault-bend folds show identical fold-limb geometries and kinematics to their forward-thrust equivalents (compare Figures 4 and 6). The simple-shear wedge case is more complex because the footwall fault-ramp is folded progressively by a footwall shear that drives strong migration of the anticlinal axial surface and limb rotation, which accounts for the different geometry of growth strata.

Shear fault-bend folding is also capable of producing wedge structures, as shown in Figure 6. Identical theories describe both the forward-thrust and wedge-thrust structures, except that, in the simple-shear end member, footwall shear deforms the fault ramp and requires a thicker shear zone, as described in Appendix A. Otherwise, the geometry and kinematics of the fold limbs are identical between the forward-thrust and wedge-thrust theories (compare Figures 4 and 6). Examples of wedge-thrust shear fault-bend folds are known from the Niger Delta (Connors et al., 1998) and from southern Taiwan (J. Suppe, 2004, unpublished works), but are not considered in this chapter.

SHEAR FAULT-BEND FOLDING THEORY

Simple-shear Fault-bend Folding

The concept of simple-shear fault-bend folding is motivated by the idea that a weak décollement layer at the base of a ramp— for example, an evaporite layer of substantial thickness— may behave more like a shear zone than like a discrete fault surface. The assumptions of the simplest possible simple-shear fault-bend-folding theory are identical to classical fault-bend folding (conserving layer thickness and bed length, with angular fault bends and fold hinges), except that a décollement layer of finite thickness undergoes an externally imposed homogeneous simple shear, α_e. Under these conditions, the backlimb dip, δ_b, is directly related to the ramp dip, θ , and the shear, α_e, by

$$\cot \alpha_e = \frac{\sin \delta_b}{2C} \left[\left[\frac{1}{\sin \delta_b \cot \theta + 1 - \cos \delta_b} \right]^2 - \left[\frac{1}{\sin \delta_b \cot \theta + 1 - \cos \delta_b} \right] \right] \quad (1)$$

where $C = 0.5$ is a parameter discussed below. A brief derivation of this equation, which is also valid for pure-shear fault-bend folding but with a different value of C, is given in Appendix A, and is from J. Suppe (2004, unpublished works). A graph of this relationship is shown in Figure 7, and a graph of the shape of a ramp anticline as a function of shear is shown in Figure 8. Note in these figures that, at very large shear— which, for example, could correspond to having a very thin décollement— the fold shape asymptotically approaches that of classical fault-bend-folding theory, with the back dip δ_b equal to the fault dip θ. The Pine Mountain thrust studied by Mitra (1988, 1992), reviewed above, lies near this asymptotic classical solution.

Pure-shear Fault-bend Folding

The concept of pure-shear fault-bend folding (Figure 4) is motivated by the idea that the deformation of

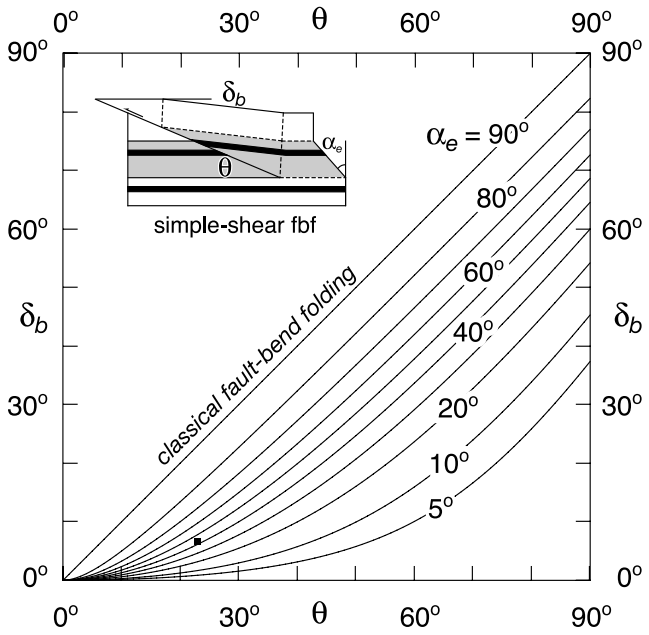

FIGURE 7. Relationship between ramp dip θ back-dip δ_b, and shear α_e for simple-shear fault-bend folding. The inset drawing of a fault ramp corresponds to the angles shown by the black square ($\theta = 23^\circ$, $\delta_b = 6.5^\circ$ and $\alpha_e = 42^\circ$).

a weak décollement layer might be confined locally to the rock volume in the immediate vicinity of a fault ramp where stresses are high, in contrast with the simple-shear end member in which shear enters the structure from the hinterland, deforming an arbitrarily large volume of rock. The theory is also motivated by observations of structures in the field (Serra, 1977) and by the results of analog and numerical mechanical models of thrust ramps with a weak décollement layer (Liu and Dixon, 1992; Liu et al., 1992; Strayer and Hudleston, 1997).

The assumptions of the simplest possible pure-shear fault-bend-folding theory are identical to those for classical fault-bend folding (conserving layer thickness and bed length, with angular fault bends and fold hinges), except that a décollement layer of finite thickness h undergoes a pure-shear shortening parallel to bedding above the ramp, with corresponding thickening perpendicular to bedding. There is an input rigid-body fault slip d with no externally imposed simple shear α_e, in contrast with simple-shear fault-bend folding (Figure 9). Thus the area of shortening of the décollement layer in the pure-shear theory is dh, which is twice the area of shortening in the homogeneous simple-shear case and which causes pure-shear folds to grow more rapidly than simple-shear folds (compare Figure 9 with Figure 7).

More generally, the area of shortening for both the pure-shear and simple-shear end members, as well as intermediate combinations of pure shear and simple shear, is

$$A_o = Cdh \tag{2}$$

where $C = 1$ for pure shear and $C = 0.5$ for homogeneous simple shear. Heterogeneous simple shear may have values of C greater or less than 0.5. Furthermore, using the appropriate numerical values of this parameter C, equation (1) more generally describes the relationship between backlimb dip δ_b, ramp dip θ, and a dimensionless input displacement or shear, $\alpha = \tan^{-1} d/h$, for both pure shear and homogeneous simple shear and intermediate combinations, as outlined in Appendix A. Figure 9 gives a graph of this relationship between limb dip δ_b and ramp dip θ as a function of input displacement, for the pure-shear case.

The pure-shear shortening and thickening of the décollement layer within the backlimb requires that the back-synclinal axial surface not bisect the syncline within the basal layer, whereas the axial surface does bisect the syncline within the overlying strata (Figure 4). The dip, ψ, (Figure 9), of the synclinal axial surface within

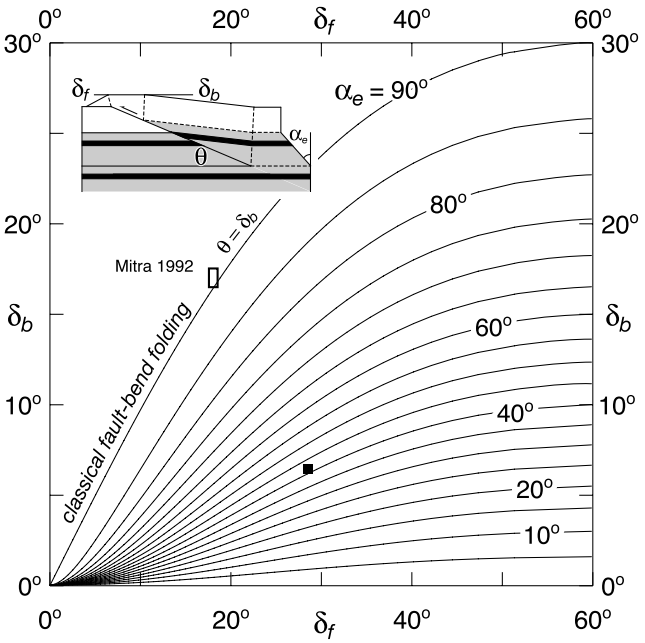

FIGURE 8. Relationship between back dip $\delta_{b'}$, front dip δ_f, and shear α_e for simple-shear fault-bend folding. The inset ramp anticline corresponds to the angles shown by the black square ($\theta = 23^\circ$, $\delta_f = 28.4^\circ$, $\delta_b = 6.5^\circ$ and $\alpha_e = 42^\circ$). Data from a cross section of the Pine Mountain thrust (Mitra, 1992) lie near the classical fault-bend folding theory ($\theta = 17^\circ$, $\delta_f = 18^\circ$, and $\delta_b = 17^\circ$), which would correspond to a décollement layer of zero thickness, and therefore $\alpha_e = 90^\circ$. The ramp dip θ is given by the curve $\alpha_e = 90^\circ$; in this case, $\theta = \delta_b$.

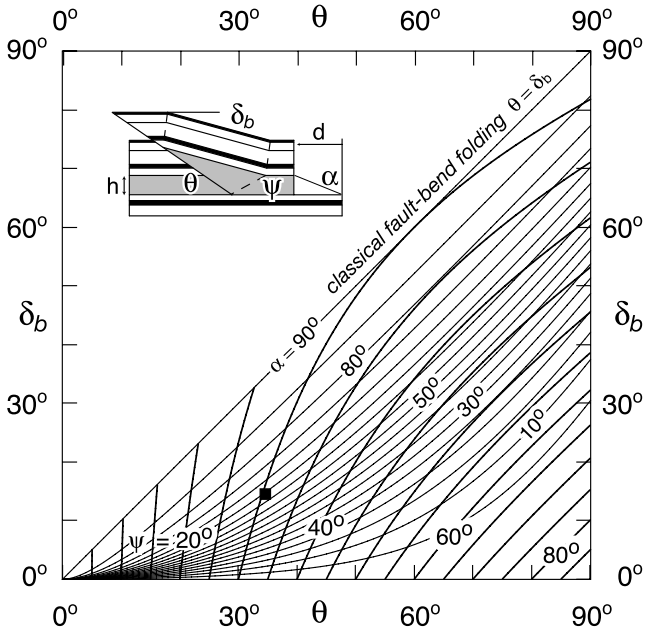

FIGURE 9. Relationship between ramp dip, θ, back-dip, δ_b, and dip of the back syncline, ψ, within the weak décollement layer for pure-shear fault-bend folding. The inset drawing of a fault ramp corresponds to the angles shown by the black square ($\theta = 34^\circ$, $\delta_b = 15.5^\circ$, $\alpha = 68^\circ$ and $\psi = 30^\circ$).

the décollement layer is given by

$$\cot\psi = 2C\left[\cot\theta + \frac{1}{\sin\delta_b} - \cot\delta_b\right] - \cot\theta \qquad (3)$$

where $C = 1$ for pure shear (see Appendix A). A graph of this equation for axial-surface dip, ψ, is given in Figure 9.

EVOLUTION OF SHEAR FAULT-BEND FOLDS

In contrast with classical fault-bend folds, shear fault-bend folds display a progressive increase in backlimb dip with increasing fault slip. This evolution is shown in Figures 10 and 11, which are graphs of backlimb dip δ_b as a function of increasing displacement d of the top of a décollement layer of finite thickness h. For

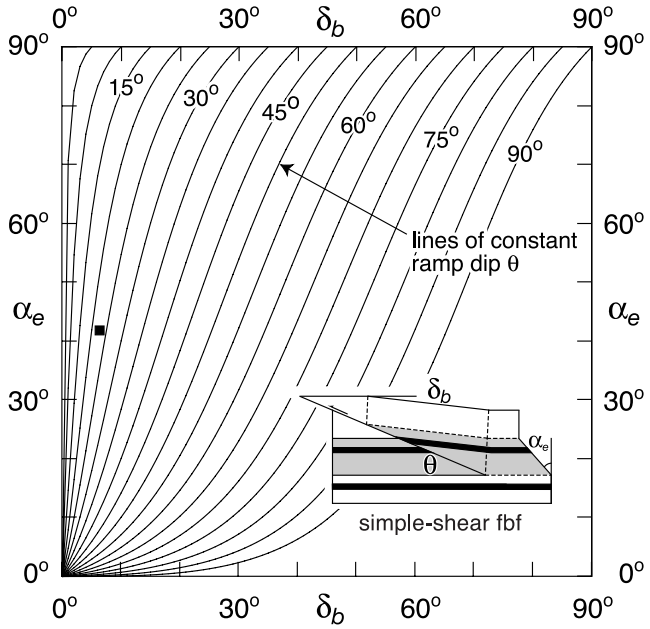

FIGURE 10. The normal evolution of simple-shear fault-bend folds is represented by lines of constant fault (ramp) dip θ (which remains constant during fold growth, unless there is footwall deformation). The backlimb dip δ_b progressively increases with increasing shear α_e until, at infinite shear $\alpha_e = 90^\circ$, the back dip δ_b asymptotically approaches the ramp dip θ. The simple-shear fault-bend fold shown as an inset has a ramp dip of 23°, therefore, it has tracked along the $\theta = 23^\circ$ curve, reaching its present back dip of $\delta_b = 6.5^\circ$ at an angular displacement of $\alpha_e = 42^\circ$.

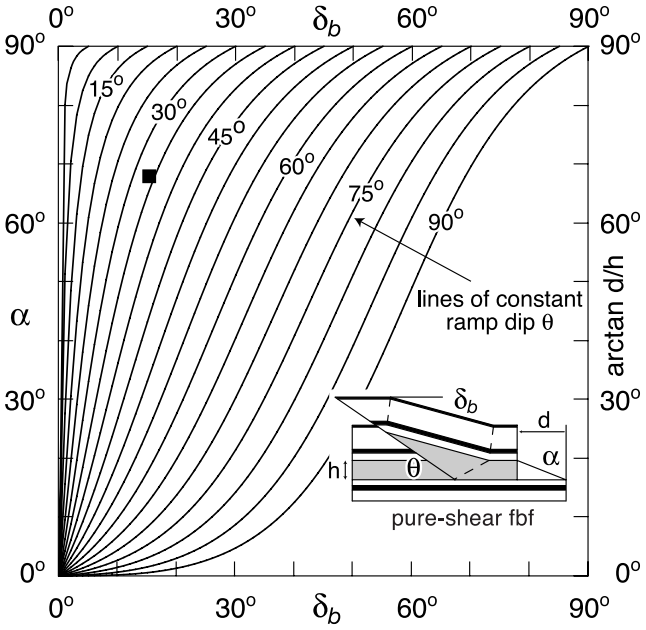

FIGURE 11. The normal evolution of pure-shear fault-bend folds is represented by lines of constant fault (ramp) dip θ (which remains constant during fold growth, unless there is footwall deformation). The backlimb dip δ_b progressively increases with increasing angular displacement (shear) $\alpha = \tan^{-1} d/h$ until, at infinite displacement d/h ($\alpha = 90^\circ$), the back dip δ_b asymptotically approaches the ramp dip θ. The pure-shear fault-bend fold shown as an inset has a ramp dip of 34°, therefore, it has tracked along the $\theta = 34^\circ$ curve, reaching its present back dip of δ_b of 15.5° degrees at an angular displacement α of 68°.

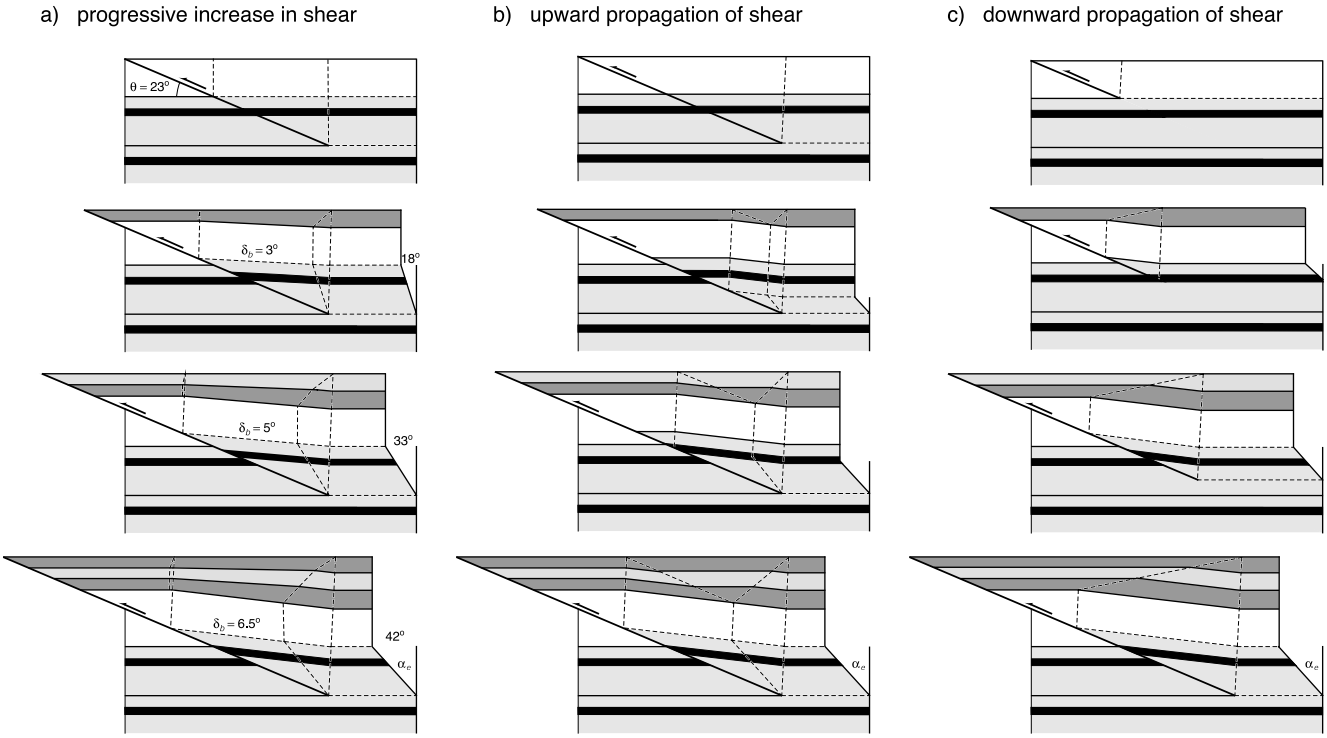

FIGURE 12. Growth models of simple-shear fault-bend folds with contrasting kinematic histories of the shear zones. (a) The left-hand drawings show a progressive increase in shear within a shear zone of constant thickness, leading to limb rotation and kink-band migration. It is the progressive change in shear that leads to limb rotation. (b) The drawings in the center show a progressive upward propagation of shear with constant angular shear, leading to kink-band migration, but no limb rotation. (c) The right-hand drawings show a progressive downward propagation of shear with constant angular shear, leading to kink-band migration of the syncline but no limb rotation.

the pure-shear fault-bend folds, as well as mixtures of pure and simple shear, this externally imposed displacement is conveniently represented in dimensionless form as an angular displacement, $\alpha = \tan^{-1} d/h$, which is immediately comparable to the externally imposed simple shear α_e in the simple-shear end member.

The evolution of any specific shear fault-bend fold normally would follow along a line of constant ramp dip, θ, as shown in these graphs (Figures 10 and 11), unless of course the ramp geometry changes with time because of footwall deformation. For example, in Figure 10 the simple-shear fault-bend fold shown as an inset in the graph has a ramp dip of 23°, therefore it has tracked along the $\theta = 23°$ curve, reaching its present back dip of $\delta_b = 6.5°$ at an angular displacement of $\alpha_e = 42°$. Note that at a very large displacement (approaching infinite shear $\alpha_e = 90°$), the backlimb dip asymptotically approaches the back dip of classical no-shear fault-bend folding, which is the ramp dip θ.

Similarly, the backlimb dips δ_b of pure-shear fault-bend folds approach the ramp dip θ at large displacement (Figure 11). For example, the pure-shear fault-bend fold shown as an inset in the graph of Figure 11 has a ramp dip of 34°, therefore it has tracked along the $\theta = 34°$ curve, reaching its present back dip δ_b of 15.5° at an angular displacement α of 68°.

GROWTH STRATA IN SHEAR FAULT-BEND FOLDS

Because of the progressive increase in both back dip and limb length, models of sedimentation over shear fault-bend folds commonly show a combination of limb rotation and kink-band migration (Figures 4 and 6). However, models of the simple-shear end member have the potential to show more variability than the pure-shear end member because of the variety of possible shear-zone kinematics. Several simple-shear models are shown as examples in Figure 12, involving (1) fixed shear-zone width with progressive increase in shear and (2) upward and (3) downward propagation of the shear zone. The progressive increase in shear causes the limb rotation. Pure-shear models display a pattern of growth strata that is similar to the fixed-thickness shear-zone models with progressive increase in shear (compare Figures 4 and 12). A seismic image from central California

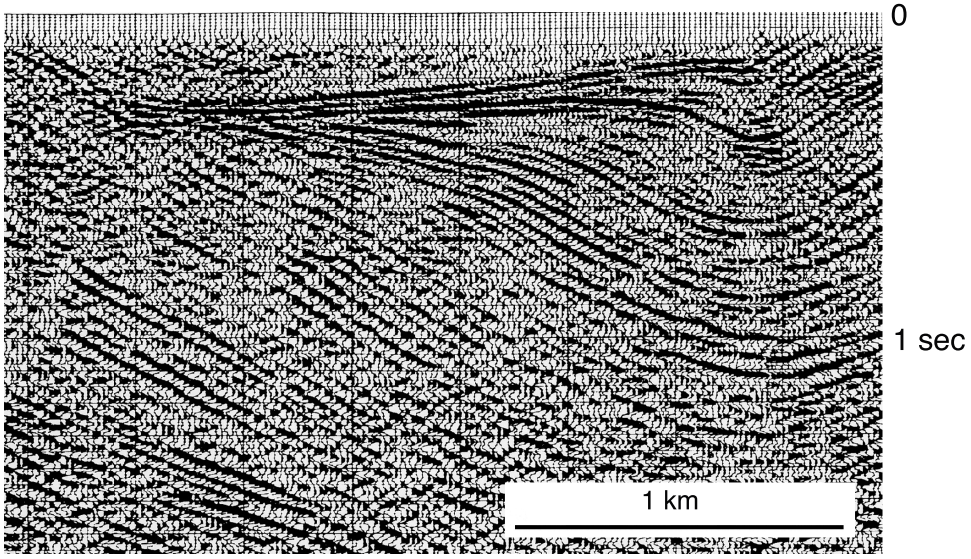

FIGURE 13. Seismic image of a fold limb, showing a combination of limb rotation and kink-band migration, similar to shear fault-bend fold models (compare Figures 4, 6, and 12), from Antelope Hills, San Joaquin Valley, California (Medwedeff, 1988). A similar seismic image showing a combination of kink-band migration and limb rotation is published by Zapata and Allmendinger (1996, *their* Figure 13) from the Bermejo anticline in Argentina.

that resembles these models, showing a combination of limb rotation and kink-band migration, is shown in Figure 13 and another from the Bermejo anticline in Argentina is published by Zapata and Allmendinger (1996, their Figure 13).

In the case of large displacement, the fold geometry in pregrowth strata approaches the geometry of classical fault-bend folding, with a backlimb dip that approaches the ramp dip. However, even in these cases growth strata may record the history of limb rotation that is characteristic of a shear fault-bend fold heritage, if the sedimentation rate is rapid enough (Figure 14).

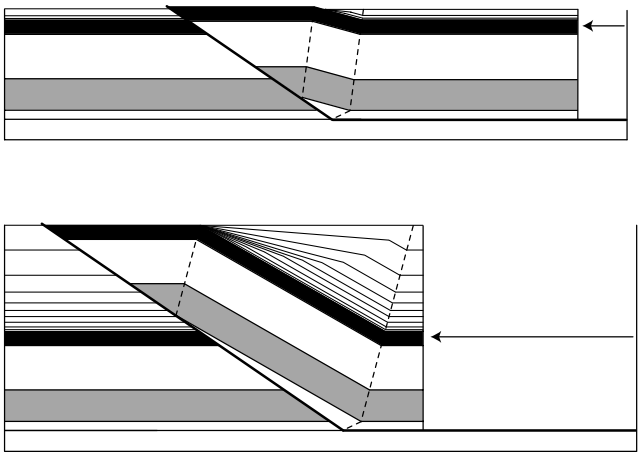

FIGURE 14. Growth model of a pure-shear fault-bend fold with large displacement such that the backlimb dip approaches the ramp dip. The geometry in pregrowth strata is similar to a classical no-shear fault-bend fold, but the limb rotation recorded in the growth strata indicates that it is a shear fault-bend fold. The sedimentation rate increases upward relative to the slip rate.

EFFECTS OF FAULT CURVATURE AND VARIABLE SHEAR

All the models shown so far have straight fault ramps of constant dip and homogeneous shear. We present several models illustrating the effects of curved fault ramps and heterogeneous simple shear to show how such complexities might be identified in data. For comparison, notice that Elliott's (1976) model (Figure 1) shows a combination of a curved fault, heterogeneous simple shear, and input fault displacement.

Figure 15 displays a set of models with a curved fault ramp. Figure 15a is a classical no-shear fault-bend fold, which requires the existence of a progressively widening curved band a–a' at the base of the ramp in which bedding in the hanging wall is parallel to the fault. In contrast, the simple-shear end member shows no such band but shows a fault slip that asymptotically reaches zero at the base of the ramp (Figure 15b and c). Therefore, the effects of fault curvature and shear are distinguishable in suitable seismic images and in models. For example, notice that such a curved band a–a' is seen in Elliott's (1976) model (Figure 1).

The effects of shear-zone thickness are also shown in Figure 15b and c. At constant displacement, the effect of increased shear-zone thickness is to reduce the limb dips above the hanging-wall cutoff of the shear zone and to reduce the area of the anticline's structural relief. Notice that the input area of shortening decreases from (a) to (c) in Figure 15.

The effects of heterogeneous simple shear are shown in Figure 16. The shear within a stratigraphic interval determines the dip of beds overlying the hanging-wall cutoff of that interval. Notice that increasing shear

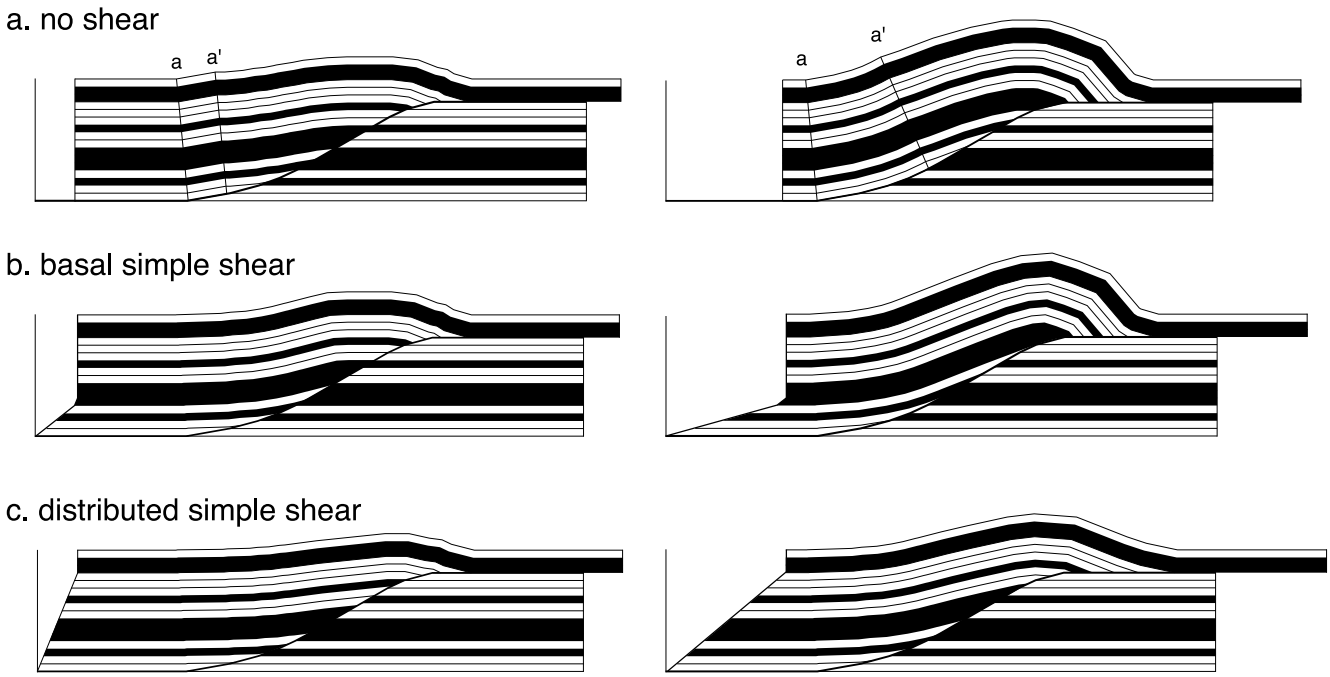

FIGURE 15. Models of curved-ramp fault-bend folding, with and without simple shear. The case of no shear (a) requires the progressive growth of a curved band a–a' at the base of the ramp, with bedding parallel to the fault, which is absent in end-member shear fault-bend folds such as (b) and (c). Also, slip goes to zero at the base of the ramp in the shear cases (b) and (c) with no bedding-parallel fault, whereas a basal fault of slip a–a' exists in the nonshear case (a). Therefore the effects of fault curvature and shear are distinguishable. Figures (b) and (c) also illustrate the effect of increasing shear zone thickness at constant displacement, which is to reduce the limb dips above the hanging-wall cutoff of the shear zone and to reduce the area of structural relief of the anticline. Notice that the input area of shortening decreases from (a) to (c).

increases the dip in the backlimb until it reaches the ramp dip at infinite shear. In contrast, increasing shear reduces the dip in the frontlimb. More generally, forward hanging-wall shear reduces the hanging-wall cutoff angle until it reaches zero at infinite shear.

TRANSMISSION OF SHEAR TO THE HINTERLAND

Models of ramp anticlines like that of Elliott (1976) (Figure 1) or the simple-shear end member (Figures 4, 15, and 16) are characterized by shear that is externally imposed— in a geometric sense— from the hinterland. Therefore, we briefly consider the implications of this hinterland transmission for the shapes of adjacent fault ramps and ramp anticlines to help us understand how this phenomenon of shear transmission could be identified in data.

If a series of foreland-propagating simple-shear fault-bend folds form on the same décollement layer, then their shear is in series and progressively adds toward the hinterland. As shown in Figure 17, the shear from a younger, more forward fold deforms both the footwall and hanging wall of an adjacent ramp in the hinterland. This reduces the backlimb dip of the hinterland structure, because both the ramp dip within the décollement layer and the effective fault-bend and cutoff angles are reduced. Thus, an additive hinterland transfer of shear should produce a distinctive pattern of hinterland reduction of ramp dips within the décollement layer, and in many cases, it should produce a reduction in backlimb dips.

However, this additive hinterland transfer of shear is not required. Just as a simple-shear fault-bend fold transforms fault slip on the ramp into shear within the décollement layer, any fault ramp in the hinterland

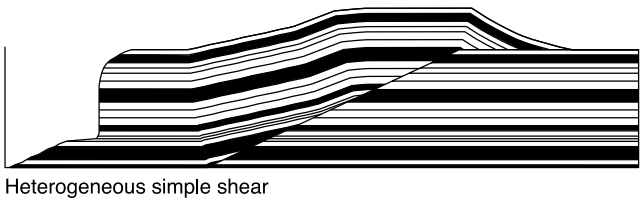

FIGURE 16. Model of simple-shear fault-bend fold with heterogeneous shear. The shear within a stratigraphic interval determines the dips of beds overlying the hanging-wall cutoff of that interval. Notice that increasing shear increases dip in the backlimb but decreases the dip in the frontlimb.

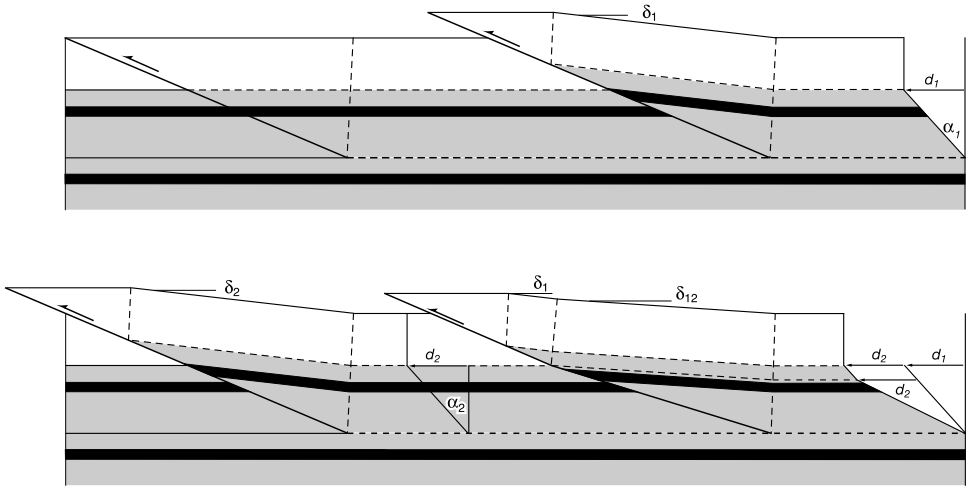

FIGURE 17. Hinterland transfer of shear. Shear from a younger simple-shear fault-bend fold toward the foreland may deform the footwall, fault ramp, and hanging wall of an adjacent fold toward the hinterland, thereby reducing its effective cutoff and ramp angles and back dip. In this model, the younger shear is transferred through the adjacent structure to produce a progressive increase in shear toward the hinterland. In contrast, Figure 18 shows a hinterland termination of shear.

can absorb that décollement shear quantitatively, as shown in Figure 18.

QUALITATIVE IDENTIFICATION OF PURE-SHEAR AND SIMPLE-SHEAR FAULT-BEND FOLDS

We can interpret candidate shear fault-bend folds by comparing them both qualitatively and quantitatively with the simple models, bearing in mind that nature might produce more-complex structures that are still fundamentally shear fault-bend folds. For example, Jordan and Noack (1992) discuss the possibility of complex heterogeneous mixtures of the end-member types involving different shear behavior of each stratigraphic level, thereby leading to more complex fold geometries. Here we point out several key qualitative features of shear fault-bend folds that will be used in our seismic interpretations below.

The most straightforward qualitative method of distinguishing the pure-shear and simple-shear end members is to observe the shape of the synclinal axial surface within the décollement layer (Figure 4). In simple-shear models the axial surface bisects the syncline because layer thickness is everywhere conserved. In contrast, the syncline's axial surface does not bisect in pure-shear models because the décollement layer thickens above the ramp. This causes the back syncline, at stratigraphic levels above the décollement layer, to be displaced toward the hinterland of the fault bend (Figure 4).

Another distinctive aspect of both end-member models is that the anticlinal axial surface marking the

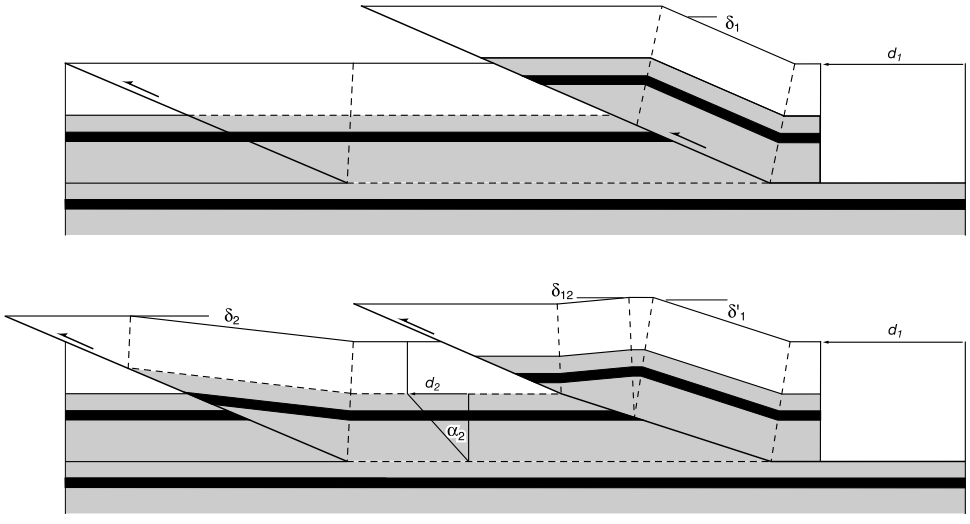

FIGURE 18. Hinterland termination of shear. In contrast with Figure 17, this model shows that shear from a younger simple-shear fault bend in the foreland can terminate at a fault in the hinterland, which might happen if the décollement layer is stronger in the hinterland or if a discrete basal fault is weak relative to the layer. Only the hanging-wall geometries differ between Figures 17 and 18; the footwall geometries are identical.

top of the back fold limb terminates at the fault at the top horizon of the décollement layer. Therefore, the inflection in dip of the syncline's axial surface should be at this same top horizon in pure-shear fault-bend folds (Figure 4). We will see this property displayed in a Nankai Trough example, below.

CASCADIA ACCRETIONARY WEDGE

Low-taper, sediment-rich accretionary wedges commonly have ramp anticlines that qualitatively resemble shear fault-bend folds. Examples are the Cascadia wedge offshore western Canada (Hyndman et al., 1994) and the Nankai wedge offshore Japan (Moore et al., 1990, 1991), both of which are shown in Figure 5. We begin by analyzing one structure from the Cascadia accretionary wedge that was well imaged as part of the Canadian Lithoprobe Project (Hyndman et al., 1994). Observe Figure 19, which is a depth-converted version of part of line 89-05. An along-strike image of the same structure in time is shown on the right-hand side of Figure 5 (line 89-04). The time section of Figure 19 was depth converted by use of a heterogeneous depth stretch based on a smoothed velocity model that incorporates velocity analysis from Yuan et al. (1994) and stacking velocities. Both seismic lines appear to be oriented within 20° of true dip direction of this structure, according to maps of Hyndman et al. (1994) and axial surface mapping (Shaw et al., 1994). In contrast, the left-hand Cascadia structure in Figure 5 is much more oblique (~40°) and hence is elongated.

The structure in Figure 19 shows a backlimb geometry that qualitatively agrees with simple-shear models (compare with Figure 4). The backlimb dip, δ_b, of 5–13° is substantially less than the ramp dip of θ = 35–40°, indicating a shear fault-bend fold with a back syncline that approximately bisects the syncline and emanates from the base of the fault ramp, which eliminates pure-shear models. The fault picks that constrain the fault geometry are shown and rule out strongly listric fault interpretations. Furthermore, fault slip goes to zero or nearly zero at the base of the ramp, indicating that no significant basal fault exists.

This structure is more complex than the simple models of Figure 4, because the fault ramp is not straight but is instead composed of two segments that dip 35° and 40°. Furthermore, the backlimb has two kink bands, *ab* and *bc,* of different dips. Let us begin by treating each segment separately. Applying the homogeneous simple-shear theory (Figure 10), we find that a backlimb dip δ_b of 11–12° within the lower kink band *ab* and a lower ramp dip θ of 35° predict an external simple shear α_e of 31–32°. The upper backlimb dip δ_b of 5° within the upper kink band *bc* together with an upper ramp dip θ of 40° predicts an external simple shear α_e of about 8°.

We test these predictions by line-length restoration of many beds in Figure 19, which shows that shear is heterogeneous on several scales. The lowest 340 m, which terminates in kink-band *ab*, has a somewhat heterogeneous shear that is overall about 31° and agrees with the 31–32° obtained from dips via theory above. The next 450 m, which terminates at the fault in kink-band *bc,* has a shear of about 8° and agrees with 8° obtained via theory. Thus the measurements from line-length restoration of many reflectors are in very good agreement with application of the homogeneous simple-shear theory to limb and fault dips.

About 120 m of growth strata has accumulated over the base of the backlimb during deformation and record limb rotation and kink-band migration (see also Figure 5). Furthermore, the reflector geometry indicates that the next shallow hinterland thrust to the right (east) deactivated just before the initiation of our structure (Figure 19).

NANKAI TROUGH ACCRETIONARY WEDGE

The frontal ramp anticline of the Nankai Trough (Figure 20) is a scientifically well-documented structure

FIGURE 19. (a) Depth-converted seismic image of part of the toe of the Cascadia accretionary wedge offshore western Canada, produced as part of the Lithoprobe Project (Hyndman et al. 1994) (line 89-05; h = v). (b) Small left-hand inset shows key fault picks that constrain the ramp geometry and indicate that it is not listric. (c) Small right-hand inset shows unfolding of the hanging wall based on conservation of bed length. The hanging wall has been unfolded to the regional dip, which allows measurement of the shear based on the deformed hanging-wall cutoff. The shear profile shows the deformation of a line originally perpendicular to bedding before deformation. An overall simple shear α_e of 31° is observed in the lowest 340 m that terminates at the fault in kink band *ab*, which agrees well with the value of 31–32° predicted via theory (Figure 10) from the backlimb dip δ_b of 11–12° for kink-band *ab* and a lower fault dip θ of 31°. A simple shear α_e of 8° is observed in the next 450 m that terminates at the fault in kink band *bc,* which agrees well with a shear of 8° predicted via theory from the backlimb dip δ_b of 5° for kink-band *bc* and an upper fault dip θ of 40°. (d) Interpreted section. Notice that fault slip goes to zero at the base of the ramp indicating that no significant bedding parallel fault exists. Shallow growth strata show limb rotation. Shallow reflector geometry indicates that growth began immediately upon termination of slip on the shallow thrust to the right (east).

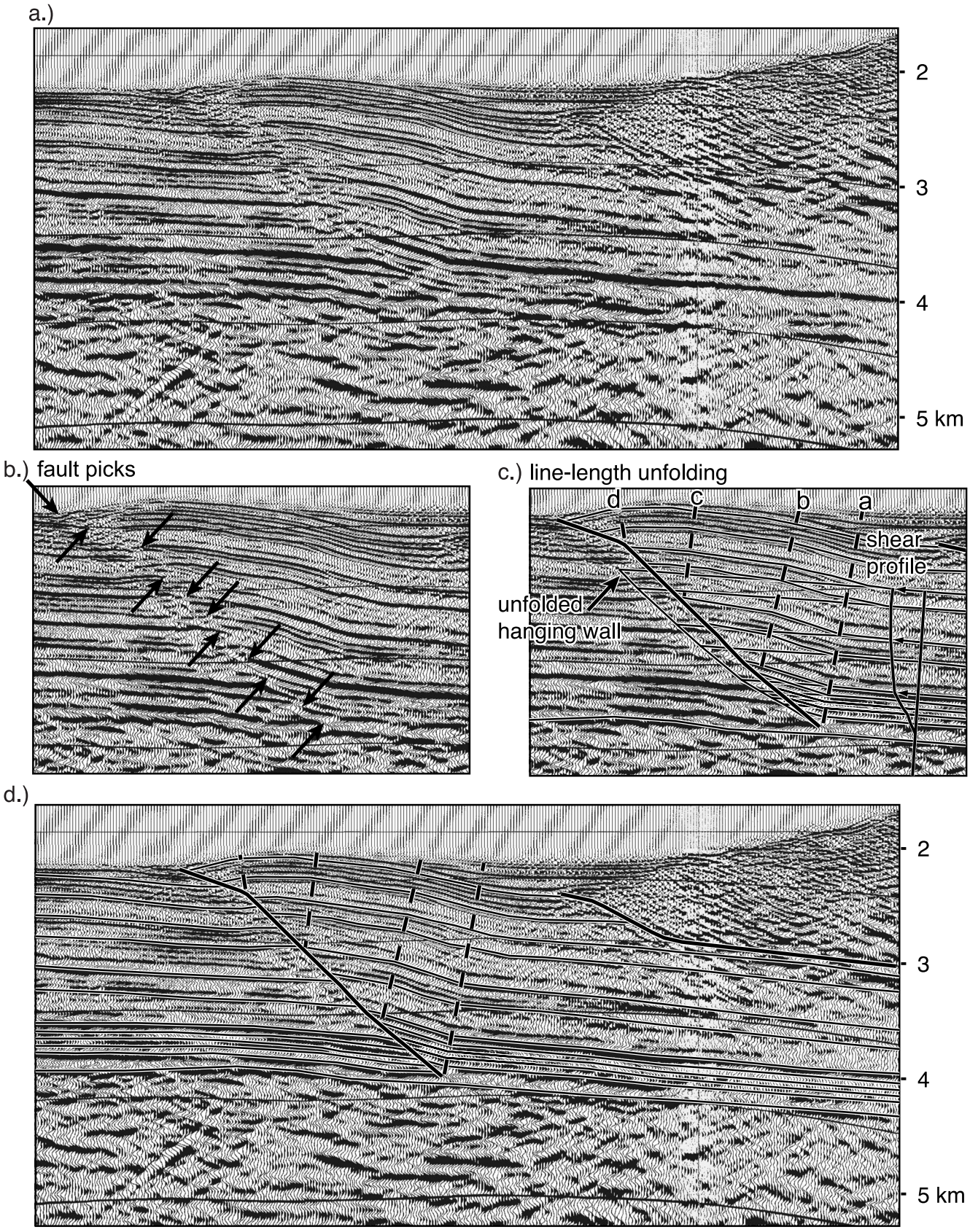
a.)
2
3
4
5 km
b.) fault picks
c.) line-length unfolding
d
c
b
a
shear
profile
unfolded
hanging wall
d.)
2
3
4
5 km

because it is the site of Ocean Drilling Project hole ODP-808/808I and extensive scientific studies in ODP Legs 131, 190, and 196. The borehole, which was extensively cored and logged, lies along the seismic line, and both the thrust ramp fault zone and the underlying décollement stratigraphic interval were cored. The depth seismic line is within 5–10° of the dip direction, as shown by Sea Beam bathymetry (Moore et al., 1991, 2001).

It should be noted that there is significant deformation prior to, and in addition to, the development of well-established dominant fault ramp structures in the front of the Nankai wedge (Figure 5). This is shown by the significant deformation of the footwall of the ODP-808 thrust and of the next seaward anticline drilled by ODP hole 1174, for which the fault ramp has yet to accumulate much displacement. Elsewhere in the Nankai Trough, Morgan et al. (1995) and Morgan and Karig (1995) have documented similar distributed deformation ahead of the frontal thrust ramp. Distributed deformation and minor wedge faulting are proportionately less significant to the total hanging-wall structure of ODP-808; nevertheless, significant wedging can be seen in the lower backlimb, similar to that in the footwall (Figure 20).

We interpreted the ODP-808 fault-ramp location based on reflector geometry and borehole data that constrain the ramp location and reflector correlations (see fault picks in Figure 20). The fault is a 60-m-wide zone with overturned beds (Tiara et al., 1991a, p. 139). Such seismic data would be interpreted traditionally with a curved, sled-runner fault geometry. However, careful examination of reflector geometry in comparison with curved fault models (Figures 1 and 15) shows that the fault cannot be substantially curved near the base of the ramp. Furthermore, recent, not-yet-published, 3-D seismic data show nearly straight faults abruptly taking off of the detachment (Gulick et al., 2000, also see Bangs et al., 1999, Moore et al., 1999, 2001). Therefore we proceed with a nearly straight-ramp interpretation (Figure 20).

The depth-migrated seismic image of the frontal thrust ramp (Figure 20) is qualitatively similar to shear fault-bend-folding models. In particular, the backlimb dip, $\delta_b \approx 13^\circ$, is substantially less than the ramp dip, $\theta = 35^\circ$. Furthermore, the back syncline in the highly reflective interval of the hanging wall is displaced substantially to the hinterland of the base of the ramp, in a way that is qualitatively similar to pure-shear fault-bend fold models, as discussed in the preceding section (compare Figure 4). Furthermore, the anticlinal axial surface at the top of the backlimb terminates at the fault at the horizon of the bend in the back syncline, in agreement with pure-shear models.

On the basis of the observed backlimb dip $\delta_b \approx 13^\circ$ and the ramp dip $\theta = 35^\circ$, we compute the dip of the back synclinal axial surface in the weak décollement layer to be $\psi = 31^\circ$. This axial surface intersects the back syncline in the overlying lid near the base of the more highly reflective interval (see pure-shear model, Figure 20). This point of intersection, according to the pure-shear model, should mark the top of the décollement interval. If we trace the horizon of intersection updip to the fault ramp, we see that it terminates at the fault at the termination of the back anticlinal axial surface, in agreement with theory. Therefore the first-order shape of the structure agrees quantitatively with the pure-shear end-member model. The back-dip and ramp angles predict a pure shear dimensionless fault slip $d/h \approx 1.7$ ($\alpha = \tan^{-1} d/h \approx 59^\circ$). The location of the top of the décollement layer yields a décollement thickness h of about 230 m, which indicates an input fault slip d of about 390 m.

Core from ODP-808 shows an intensely deformed basal detachment zone that is 19 m thick (Moore et al., 1991; Tiara et al., 1991b). Overlying strata that would correspond to the stratigraphic interval of the décollement layer of the pure-shear interpretation is composed of Shikoku Basin muds, and the overlying, more highly reflective interval is composed of Shikoku Basin turbidites. Analysis of faulting in ODP-808 core and

Figure 20. (a) Depth-migrated seismic image of the toe of the Nankai Trough accretionary wedge at Ocean Drilling Project site ODP-808, offshore Japan (Moore et al., 1991) (line NT62-8; h = v). (b) The small left-hand figure shows constraints on fault-ramp location based on reflector geometry at locations shown by arrows and by the location in ODP-808 core. (c) Small right-hand figure shows best-fitting pure-shear model discussed in text. (d) Annotated seismic image showing key observations indicating a pure-shear fault-bend fold origin. Note that the shallow structure is somewhat detached. The deep backlimb geometry qualitatively agrees with pure-shear models (compare Figure 4) with a backlimb dip $\delta_b = 11–13^\circ$ that is less than the ramp dip $\theta = 35^\circ$ and a back syncline that is displaced substantially to the hinterland of the fault bend, which eliminates simple-shear models. Simple-shear models are less favored by the observation of a 19-m-thick detachment zone observed in the ODP-808 core. The backlimb dip $\delta_b \approx 13^\circ$ and ramp dip $\theta = 35^\circ$ yield a pure-shear fault-bend fold prediction of the back synclinal axial surface in the décollement layer of $\psi = 31^\circ$, which quantitatively agrees with the seismic image as shown in the right-hand figure. The location of the top of the décollement is indicated by the inflection in the back syncline, which agrees with the location indicated by the fault cutoff of the back anticline, as predicted by pure-shear models (compare Figure 4). The back-dip and ramp angles predict a pure shear dimensionless fault slip $d/h = 1.7$ ($\alpha = \tan^{-1} d/h \approx 59^\circ$). The location of the top of the décollement layer yields a décollement thickness h of about 230 m, which indicates an input fault slip d of about 390 m.

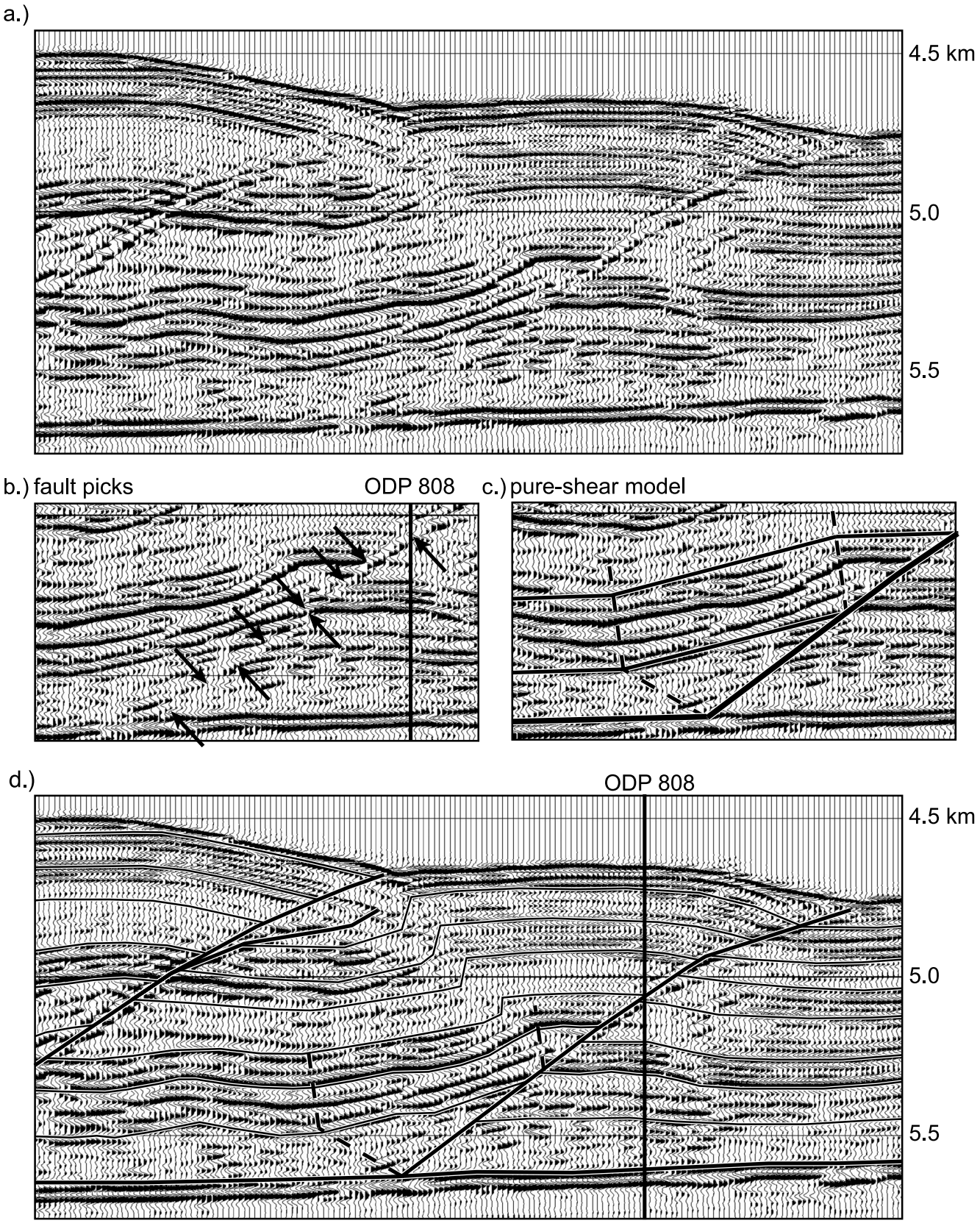
a.)
4.5 km
5.0
5.5
b.) fault picks
ODP 808
c.) pure-shear model
d.)
ODP 808
4.5 km
5.0
5.5

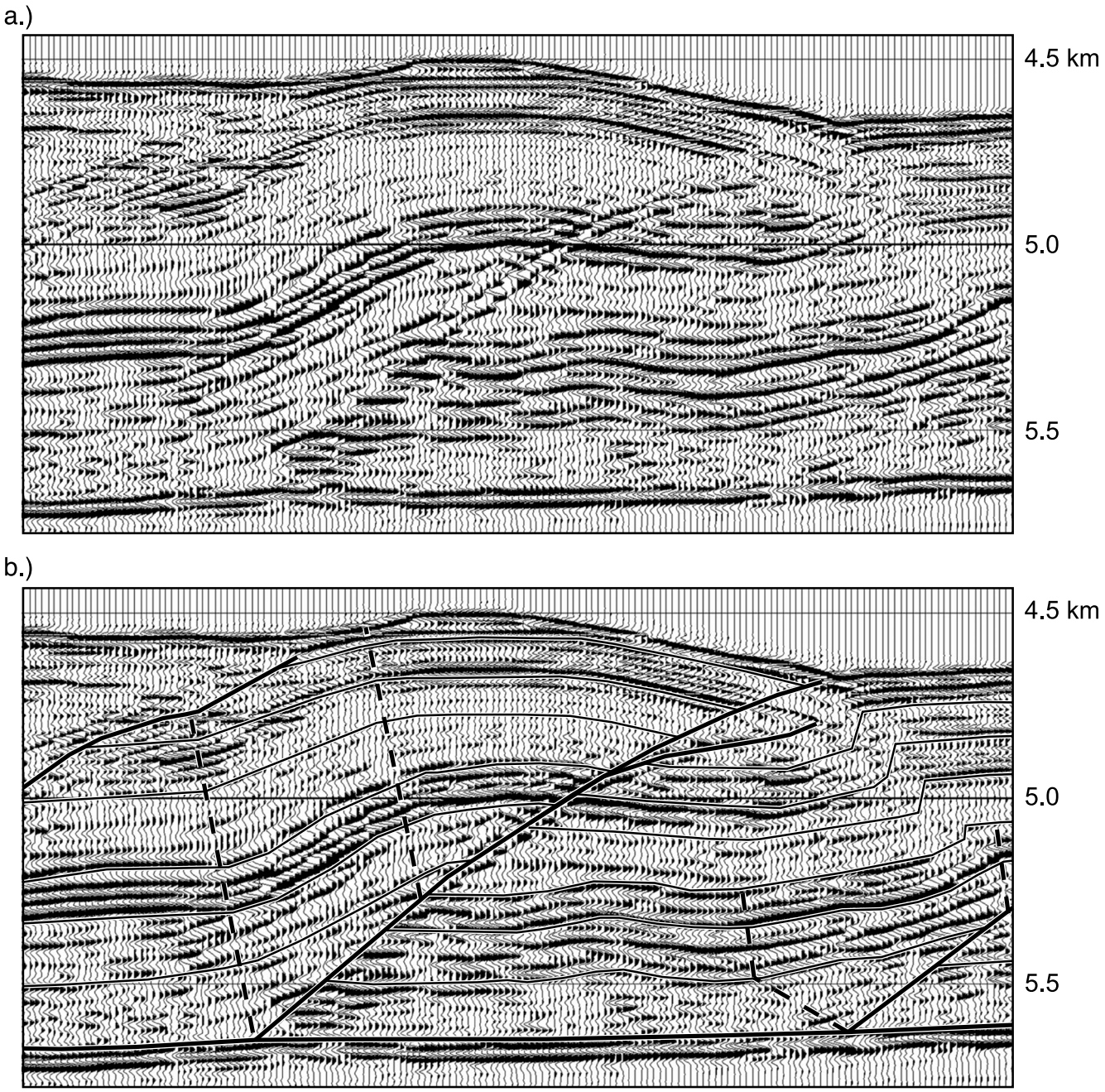

Figure 21. (a) Depth-migrated seismic image of structure just interior to that of Figure 20 (Moore et al. 1991) (line NT62-8; h = v). (b) Annotated seismic showing a backlimb geometry that qualitatively agrees with simple-shear models (compare Figure 4). The backlimb dip δ_b = 23–25° is less than the ramp dip θ = 39°, and the back syncline approximately bisects the syncline and emanates from the fault bend, which eliminates pure-shear models. The backlimb dip δ_b = 23–25° and ramp dip θ = 39° predict a simple shear of α_e = 60–65°. The stratigraphic level of the top of the shear zone is indicated by the fault cutoff of the back anticline, as shown by simple-shear models (compare Figure 4), which yields a décollement thickness h of about 190 m. The displacement of the top of the shear zone is therefore $d = h \tan \alpha_e$, or about 330–410 m.

image logging indicates a higher density of faulting below the turbidites (Tiara et al., 1991a, Figure 155; Shipboard Scientific Party 2001).

The next thrust ramp to the north of ODP-808 (Figure 21) shows a similar ramp dip but a substantially different hanging-wall geometry that qualitatively agrees with simple-shear models (compare Figure 4). The backlimb dip δ_b = 23–25° is less than the ramp dip θ = 39°, indicating a shear fault-bend fold, but the fact that the back syncline approximately bisects the syncline and

emanates from the fault bend eliminates pure-shear models. Furthermore, the steepness of the backlimb qualitatively indicates very substantial shear, indeed, more than in the Cascadia example, which had a similar ramp dip of 35–40° but limb dips of only 5° and 12° at two stratigraphic levels, thereby indicating shears α_e of 8° and 31° (Figure 19).

Applying the simple-shear theory (Figure 10), we find that a backlimb dip δ_b of 23–25° together with a ramp dip θ of 40° predicts a simple shear α_e of about 63–67°. Furthermore, the stratigraphic level of the top of the shear zone is indicated by the fault cutoff of the back anticlinal axial surface (as shown by simple-shear models— compare Figure 4), which yields a décollement thickness h of about 190 m and is therefore similar to that of the previous structure. The displacement d of the top of the shear zone is $h \tan \alpha_e$, or about 330–410 m. This very substantial shear, of α_e = 63–67°, of course requires substantial transfer of shear toward the hinterland. Unfortunately, the structures to the north are not well imaged and we cannot test this implication at present.

DISCUSSION

Shear fault-bend folding produces very distinctive geometries for ramp anticlines. They are characterized by long, gentle backlimbs that dip less than the fault ramp does, in contrast with classical fault-bend folding. Backlimb dips and limb lengths progressively increase with fault slip, by a combination of limb rotation and kink-band migration. Application of simple end-member shear fault-bend fold models to depth-seismic images from the Nankai Trough and Cascadia accretionary wedges shows agreement between theory and data, with substantial shear (α = 40–65°) over stratigraphic intervals a few hundred meters thick. Furthermore, the structural styles of many ramp anticlines in the compressive toe of the deep-water Niger Delta are qualitatively very similar to shear fault-bend fold models (Connors et al., 1998). Therefore, we suggest that shear fault-bend fold concepts may have wide applicability, in spite of their limited application to date. Shear fault-bend folding may be particularly relevant at the toes of passive margins, which are important areas of present-day oil exploration.

ACKNOWLEDGMENTS

We are especially grateful to Roy D. Hyndman of the Pacific Geoscience Centre for providing us with copies of the Cascadia seismic lines, and to Greg F. Moore of the University of Hawaii for providing the Nankai Trough line. We are also extremely grateful for the very careful and thoughtful reviews of the manuscript by Josep Poblet of the University of Oviedo and Dave Waltham of Royal Holloway. The final manuscript was substantially improved because of their stimulating reviews. Finally, we take pleasure in thanking Ken R. McClay for having the vision and energy to host three stimulating Thrust Tectonics conferences and to see the volumes through to publication.

APPENDIX A

We present here a brief derivation of the simple-shear and pure-shear fault-bend folding theories, as a single combined theory following J. Suppe (2004, unpublished works), using the geometric elements shown in Figures 22 and 23. The theory is conceptually similar to that of Jordan and Noack (1992) but differs substantially in detail. A thrust steps up from a bedding-parallel detachment at an angle θ. There is a basal deformable layer of original thickness h that is allowed either to (1) undergo homogeneous simple shear parallel to bedding or (2) to shorten and thicken to h' within the backlimb by pure shear parallel to bedding. In contrast, the overlying strata undergo no externally applied simple shear and instead conserve bed length and layer thickness.

We now apply the constraints of conservation of bed length and area, and of continuity, to obtain the basic equations of simple-shear and pure-shear fault-bend folding. The two theories are end members differing only by the numerical value of a parameter C that describes the area of shortening of the basal deformable layer after a displacement d of its top from q to q'

$$A_o = Cdh \tag{4}$$

where C = 1/2 for homogeneous simple shear and C = 1 for pure shear. Other values of C are possible because of heterogeneity or because of mixtures of end members, but here we only consider the two special cases.

For purposes of the derivation, we partition the deformation into an imaginary horizontal displacement followed by folding. The geometry after a horizontal simple shear $\alpha_e = \tan^{-1} d/h$ is shown in the bottom of Figure 22. In the pure-shear case, the geometry after the same horizontal displacement d is shown in the bottom of Figure 23, for which the same function $\alpha = \tan^{-1} d/h$ can be defined. The hanging-wall cutoff of the top of the basal deformable layer is displaced a distance d, from r to r, producing an area of shortening of $A_o = dh/2$ in the homogeneous simple-shear case and $A_o = dh$ in the pure-shear case, which is the area of overlap between the hanging wall and footwall in our imaginary state before folding.

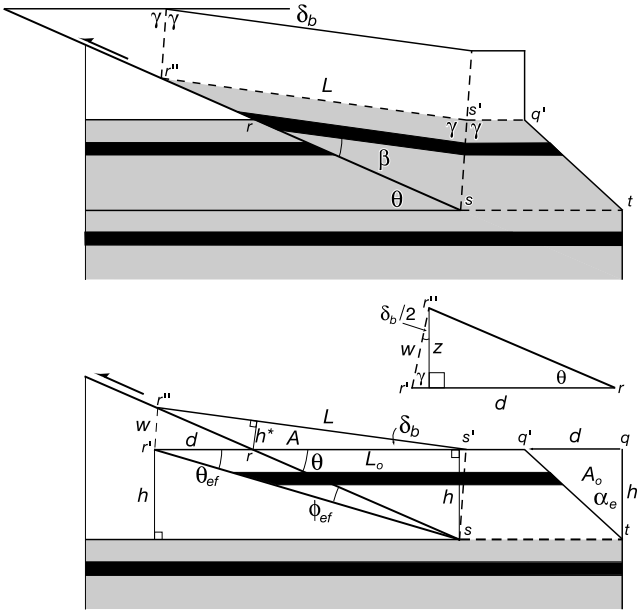

FIGURE 22. Geometric elements used in the derivation of the simple-shear fault-bend folding theory (after J. Suppe, 2004, unpublished works). The present deformed shape is shown in the top drawing, with a ramp dip θ, backlimb dip δ_b, and limb length L at the top of a basal layer of thickness h. The derivation factors the deformation into two nonphysical steps shown in the bottom drawing. (1) An external shear, α_e, is applied before folding of the hanging-wall block, to modify the initial cutoff angle θ to an effective cutoff angle θ_{ef} and to create an effective fault bend ϕ_{ef}. (2) The hanging wall is then folded by flexural slip; in particular, the bed segment L_o at the top of the basal layer is rotated to become the backlimb of length L. The folded hanging wall conforms to the fault, with no voids or overlap, subject to several balancing constraints. The area of shortening, A_o, is constrained to be equal to the area of structural relief A and to the area of overlap before folding (area of triangle $\Delta rr's$). There is conservation of layer thickness across axial surfaces ($\gamma = 90^\circ - \delta_b/2$), and bed length is conserved ($L_o = L$). The middle drawing is an enlargement of the details of triangle $\Delta rr'r''$ in the bottom drawing.

After folding, there is no overlap. The hanging-wall cutoff of the top of the deformable basal layer is displaced a distance w, from r' to r'', such that the bed segment $r's' = L_o$ is rotated to become $r''s' = L$ with a limb dip δ_b, as is shown in the bottom of Figures 22 and 23.

By applying conservation of bed length to triangle $\Delta r'r''s'$ we get

$$w = 2L\sin(\delta_b/2) \tag{5}$$

and by applying the law of sines to triangle $\Delta rr'r''$ we get

$$\frac{\cos((\delta_b/2) - \theta)}{d} = \frac{\sin\theta}{2L\sin(\delta_b/2)} = \frac{\sin\gamma}{rr''}. \tag{6}$$

Simplifying, we obtain the ratio of displacement d to deformed limb length L

$$d/L = \sin\delta_b\cot\theta + 1 - \cos\delta_b. \tag{7}$$

By constraining the area of structural relief A to be equal to the area of shortening, $A_o = Cdh$, we have

$$A = Cdh = L(L-d)\frac{\sin\delta_b}{2} \tag{8}$$

and

$$\cot\alpha = \frac{h}{d} = \frac{\sin\delta_b}{2C}\left[\left[\frac{L}{d}\right]^2 - \left[\frac{L}{d}\right]\right]. \tag{9}$$

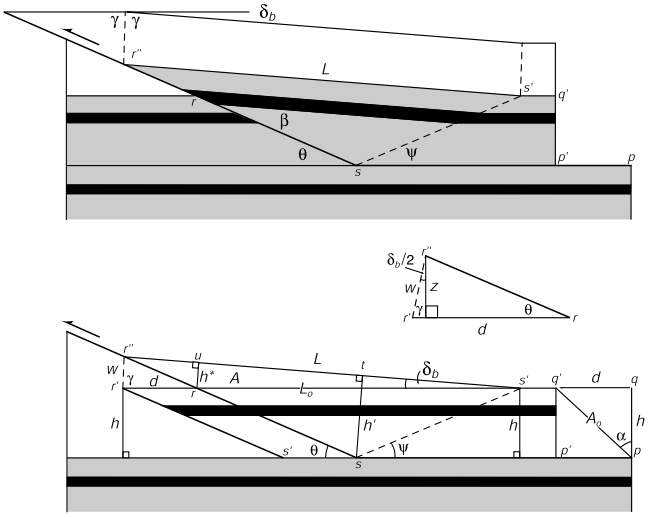

FIGURE 23. Geometric elements used in the derivation of pure-shear fault-bend folding theory (after J. Suppe, 2004, unpublished works). The present deformed shape is shown in the top drawing, with a ramp dip θ, backlimb dip δ_b, and limb length L at the top of a basal deformable layer of initial thickness h. The derivation factors the deformation into two nonphysical steps shown in the bottom drawing. (1) A dimensionless fault slip, $\alpha = \tan^{-1}d/h$, is applied before folding of the hanging-wall block, to produce an overlap of the footwall of area $A_o = dh$ (area of parallelogram $rr's's$). (2) The hanging wall is then folded by shortening and thickening of the basal layer in bedding-parallel pure shear above the ramp, reaching a thickness h'. In particular, the bed segment L_o at the top of the basal layer is rotated to become the back limb of length L. The folded hanging wall conforms to the fault, with no voids or overlap, subject to several balancing constraints. The area of shortening A_o is constrained to be equal to the area of structural relief A and to the area of overlap before folding. There is continuity of layers across the back syncline in the deformable basal layer, such that $h'/h = \sin(\psi + \delta_b)/\sin\psi$. Above this basal layer, there is conservation of layer thickness across axial surfaces ($\gamma = 90^\circ - \delta_b/2$), and bed length is conserved ($L_o = L$). The middle drawing is an enlargement of the details of triangle $\Delta rr'r''$ in the bottom drawing.

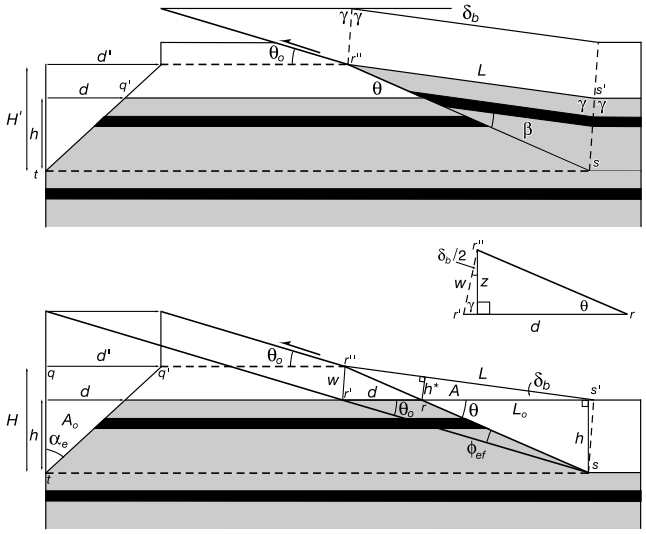

FIGURE 24. Geometric elements used in the derivation of the wedge simple-shear fault-bend fold theory (after J. Suppe, 2004, unpublished works). The present deformed shape is shown in the top drawing, with a deformed ramp dip θ, undeformed ramp dip θ_o, backlimb dip $\delta_{b'}$, and limb length L at the top of a basal layer of initial thickness h. The derivation factors the deformation into two nonphysical steps shown in the bottom drawing. (1) An external shear α_e, is applied to the footwall before folding of the hanging-wall block, to modify the initial cutoff angle θ_o to the deformed cutoff angle θ and create an effective fault bend ϕ_{ef}. After shear, the fault has a change in dip at point r''. The footwall shear zone has a thickness H' and a displacement d'. (2) The hanging wall is then folded by flexural slip. In particular, the bed segment L_o at the top of the basal layer is rotated to become the backlimb of length L. The geometry and kinematics of the fold limb in the hanging-wall are substantially different from the case of hanging-wall shear (Figure 22). This is because there is progressive deformation of the fault, which drives rapid migration of the fault bend (point r''), thereby producing distinctive growth stratal geometries (Figure 6). The middle drawing is an enlargement of the details of triangle $\Delta rr'r''$ in the bottom drawing.

Combining with (7)

$$\cot\alpha = \frac{\sin\delta_b}{2C}\left[\left[\frac{1}{\sin\delta_b\cot\theta + 1 - \cos\delta_b}\right]^2 - \left[\frac{1}{\sin\delta_b\cot\theta + 1 - \cos\delta_b}\right]\right] \qquad (10)$$

which is the same as (1), the basic equation for dimensionless displacement α as a function of ramp dip θ and limb dip δ_b. The parameter $C = A_o/dh$ is 1 for pure-shear and 1/2 for homogeneous simple-shear.

In the simple-shear case, the back syncline within the basal deformable layer bisects the fold hinge at an angle $\gamma = 90^\circ - \delta_b/2$, reflecting the fact that layer thickness is conserved. In contrast, in the pure-shear case, the basal deformable layer of original thickness h is allowed to shorten and thicken to h' within the backlimb, by pure shear parallel to bedding, whereas the overlying strata conserve bed length and layer thickness.

By continuity of bedding across the back synclinal axial surface of orientation ψ,

$$\frac{h'}{h} = \frac{\sin(\psi + \delta_b)}{\sin\psi}. \qquad (11)$$

By conservation of area in the deformed backlimb,

$$\frac{1}{2}h'L = \frac{1}{2}h(L - d) + Cdh \qquad (12)$$

and by combining with (7) and (11) we have

$$\cot\psi = 2C\left[\cot\theta + \frac{1}{\sin\delta_b} - \cot\delta_b\right] - \cot\theta \qquad (13)$$

which is the same as (3), the basic equation for the orientation of the back synclinal axial surface ψ as a function of ramp dip θ and limb dip δ_b. In the pure-shear case ($C = 1$), equation (13) reduces to

$$\cot\psi = \cot\theta + 2\tan\delta/2 = \cot\theta + 2\cot\gamma \qquad (14)$$

and in the homogeneous simple-shear case ($C = 1/2$), it reduces to

$$\cot\psi = \tan\delta/2 = \cot\gamma$$

and

$$\psi = 90^\circ - \delta/2 = \gamma. \qquad (15)$$

The equations outlined above also hold for footwall wedges, producing identical fold-limb geometry and, in the pure-shear case, identical kinematics (compare Figures 4 and 6). However, in the simple-shear wedge case, the fault is deformed and the shear zone is thicker, H, than in the forward simple-shear case, h, because of footwall shear (see Figures 6 and 24). The undeformed fault dip θ_o of the simple-shear wedge is

$$\cot\theta_o = \tan\alpha_e + \cot\theta. \qquad (16)$$

The fault slip rr'' is from equation (6)

$$rr'' = \frac{d \sin\gamma}{\cos((\delta_b/2) - \theta)} = \frac{h \tan\alpha_e \cos(\delta_b/2)}{\cos((\delta_b/2) - \theta)}$$

$$= \frac{h \tan\alpha_e}{\cos\theta + \tan(\delta_b/2)\sin\theta} \quad (17)$$

and the total thickness of the footwall shear zone is

$$H = z + h = rr'' \sin\theta + h = h\left[\frac{\tan\alpha_e}{\cot\theta + \tan(\delta_b/2)} + 1\right]. \quad (18)$$

REFERENCES CITED

Bangs, N. L., A. Taira, S. Kuramoto, T. H. Shipley, G. F. Moore, K. Mochizuki, S. S. Gulick, Z. Zhao, Y. Nakamura, J. O. Park, et al., 1999, U.S.-Japan collaborative 3-D seismic investigation of the Nankai Trough plate-boundary interface and shallowmost seismogenic zone: EOS, Transactions of the American Geophysical Union, v. 80, p. F569.

Connors, C. D., D. B. Denson, G. Kristiansen, and D. M. Angstadt, 1998, Compressive anticlines of the mid-outer slope, central Niger Delta: AAPG Bulletin, v. 82, p. 1903.

Davis, D., J. Suppe, and F. A. Dahlen, 1983, Mechanics of fold-and-thrust belts and accretionary wedges: Journal of Geophysical Research, v. 88, p. 1153–1172.

Elliott, D., 1976, The motion of thrust sheets: Journal of Geophysical Research, v. 81, p. 949–963.

Gulick, S. P., N. L. Bangs, T. H. Shipley, Z. Zhao, Y. Nakamura, G. F. Moore, S. Kuramoto, A. Taira, D. J. Hills, and J. Park, 2000, 3-D structural geometry and fluid flow indicators from the 1st out-of-sequence thrust to the deformation front of the Nankai accretionary prism: preliminary results from the Nankai Trough 3-D Seismic Experiment: EOS, Transactions of the American Geophysical Union, v. 81, p. F1067.

Hyndman, R. D., G. D. Spence, T. Yuan, and E. E. Davis, 1994, Regional geophysics and structural framework of the Vancouver Island margin accretionary prism: Proceedings of the Ocean Drilling Program, Part A: Initial Reports, v. 146, p. 399–419.

Jamison, W. R., 1987, Geometric analysis of fold development in overthrust terranes: Journal of Structural Geology, v. 9, p. 207–219.

Jordan, P., and T. Noack, 1992, Hangingwall geometry of overthrusts emanating from ductile décollements, *in* K. R. McClay, ed., Thrust tectonics: London, Chapman & Hall, p. 311–318.

Liu S., and J. Dixon, 1992, Centrifuge modelling of the propagation of thrust faults, *in* K. R McClay, ed., Thrust tectonics: London, Chapman & Hall, p. 53–69.

Liu H., K. R McClay, and D. Powell, 1992, Physical models of thrust wedges, *in* K. R McClay, ed., Thrust tectonics: London, Chapman & Hall, p. 71–81.

Malavieille, J., and J. F. Ritz, 1989, Mylonitic deformation of evaporites in décollements: examples from the Southern Alps, France: Journal of Structural Geology, v. 11, p. 583–590.

Medwedeff, D. A., 1988, Structural analysis and tectonic significance of late-Tertiary and Quaternary compressive growth folding, San Joaquin Valley, California: Ph.D. Dissertation, Princeton University, 184 p.

Mitra, S., 1988, Three-dimensional geometry and kinematic evolution of the Pine Mountain thrust system, Southern Appalachians: Geological Society of America Bulletin, v. 100, no. 1, p. 72–95.

Mitra, S., 1990, Fault-propagation folds: geometry, kinematic evolution, and hydrocarbon traps: AAPG Bulletin, v. 74, no. 6, p. 921–945.

Mitra, S., 1992, Balanced structural interpretations in fold and thrust belts, *in* S. Mitra and G. W. Fischer, eds., Structural geology of fold and thrust belts: Baltimore, The Johns Hopkins University Press, p. 53–77.

Mitra, S., and J. Namson, 1989, Equal-area balancing: American Journal of Science, v. 289, p. 563–599.

Moore, G. F., T. H. Shipley, P. L. Stoffa, D. E. Karig, A. Taira, S. Kuramoto, H. Tokuyama, and K. Suyehiro, 1990, Structure of the Nankai Trough accretionary zone from multichannel seismic reflection data: Journal of Geophysical Research, v. 95, p. 8753–8765.

Moore, G. F., D. E. Karig, T. H. Shipley, A. Taira, P. L. Stoffa, and W. T. Wood, 1991, Structural framework of the ODP Leg 131 area, Nankai Trough: Proceedings of the Ocean Drilling Program, Part A: Initial Reports, v. 131, p. 15–20.

Moore, G. F., A. Taira, S. Kuramoto, T. H. Shipley, and N. L. Bangs, 1999, Structural setting of the 1999 U.S.-Japan Nankai Trough 3-D seismic reflection survey: EOS, Transactions of the American Geophysical Union, v. 80, p. F569.

Moore, G. F., A. Taira, N. L. Bangs, S. Kuramoto, T. H. Shipley, C. M. Alex, S. S. Gulick, D. J. Hills, T. Ike, S. Ito, et al., 2001, Data report: structural setting of the Leg 190 Muroto transect, *in* Moore, G. F., Taira, A., Klaus, A., et al., Proceedings of the Ocean Drilling Program, Initial Reports v. 190. ⟨http://www-odp.tamu.edu/publications/190_IR/chap_02/chap_02.htm⟩, (accessed February 2003).

Morgan, J. K., D. E. Karig, and A. Maniatty, 1995, The estimation of diffuse strains in the toe of the western Nankai accretionary prism; a kinematic solution: Journal of Geophysical Research, v. B99, p. 7019–7032.

Morgan, J. K., and D. E. Karig, 1995, Kinematics and a balanced and restored cross-section across the toe of the eastern Nankai accretionary prism: Journal of Structural Geology, v. 17, p. 31–45.

Mosar, J., and J. Suppe, 1991, Role of shear in fault-propagation folding, *in* K. R. McClay, ed., Thrust tectonics: London, Chapman & Hall, p. 123–132.

Poblet, J., and K. McClay, 1996, Geometry and kinematics of single-layer detachment folds: AAPG Bulletin, v. 80, p. 1085–1109.

Serra, S., 1977, Styles of deformation in the ramp regions of overthrust faults: Wyoming Geological Association Guidebook, 29th Annual Field Conference, p. 487–498.

Shaw, J. H., S. C. Hook, and J. Suppe, 1994, Structural trend analysis by axial surface mapping: AAPG Bulletin, v. 78, p. 700–721.

Shipboard Scientific Party, 2001, Leg 196 Preliminary Report: Deformation and fluid flow processes in the Nankai Trough accretionary prism: logging while drilling and advanced CORKs. Ocean Drilling Project Preliminary Report, v. 96 [Online]. ⟨http://www-odp.tamu.edu/publications/prelim/196_rel/196PREL.PDF⟩.

Storti, F., and J. Poblet, 1997, Growth stratal architectures associated to décollement folds and fault-propagation folds; inferences on fold kinematics: Tectonophysics, v. 282, p. 353–373.

Strayer, L., and P. Hudleston, 1997, Numerical modeling of fold initiation at thrust ramps: Journal of Structural Geology, v. 19, p. 551–566.

Suppe, J.,1983, Geometry and kinematics of fault-bend folding: American Journal of Science, v. 283, p. 684–721.

Suppe, J., 1984, Seismic interpretation of compressively reactivated normal fault near Hsinchu, western Taiwan: Petroleum Geology of Taiwan, no. 20, p. 85–96.

Suppe, J., and D. A. Medwedeff, 1990, Geometry and kinematics of fault-propagation folding: Eclogae Geologicae Helvetiae, v. 83 (Laubscher vol.), p. 409–454.

Suter, M., 1981, Strukturelles Querprofil durch den nordwestlichen Faltenjura, Mt-Terri-Randüberschiebung-FreibergeL: Eclogae Geologicae Helvetiae, v. 74, p. 255–275.

Taboada, A., J. F. Ritz, and J. Malavieillie, 1990, Effect of ramp geometry on deformation in a ductile décollement level: Journal of Structural Geology, v. 12, p. 297–302.

Tamagawa, T., T. Matsuoka, and Y. Tamura, 1998, Geometrical shape of fault-bend folding with simple shear deformation in the thrust sheet (in Japanese): Geoinformatics (Joho Chishitsu, Osaka), v. 9, p. 3–11.

Tiara, A., I. Hill, J. V. Firth, et al., 1991a, Site 808: Proceedings of the Ocean Drilling Program, Part A: Initial Reports, v. 131, p. 71–269.

Tiara, A., I. Hill, J. V. Firth, et al., 1991b, Sediment deformation and hydrogeology at the Nankai accretionary prism: synthesis of ODP Leg 131 shipboard results: Proceedings of the Ocean Drilling Program, Part A: Initial Reports, v. 131, p. 273–285.

Yuan, T., G. D. Spence, and R. D. Hyndman, 1994, Seismic velocities and inferred porosities in the accretionary wedge sediments at the Cascadia margin: Journal of Geophysical Research, v. 99, p. 4413–4427.

Zapata, T., and R. W. Allmendinger, 1996, Growth stratal records of instantaneous and progressive limb rotation in the Precordillera thrust belt and Bermejo basin, Argentina: Tectonics, v. 15, p. 1065–1083.